Mycobacterial Metallophosphatase MmpE Acts as a Nucleomodulin to Regulate Host Gene Expression and Promote Intracellular Survival

Liu Chen[1,2], Baojie Duan[1], Qiang Jiang[1], Yifan Wang[1], Yingyu Chen[1,3], Lei Zhang[1,3]* and Aizhen Guo[1,2,3]*

[1] National Key Laboratory of Agricultural Microbiology, College of Veterinary Medicine, Huazhong Agricultural University, Wuhan 430070, China

[2] Hubei Hongshan Laboratory, Huazhong Agricultural University, Wuhan 430070, China

[3] National Professional Laboratory for Animal Tuberculosis, Ministry of Agriculture and Rural Affairs, Huazhong Agricultural University, Wuhan 430070, China

*Address correspondence to: Lei Zhang, zhanglei2023@mail.hzau.edu.cn; Aizhen Guo, aizhen@mail.hzau.edu.cn

Abstract

Mycobacterium tuberculosis, the causative agent of tuberculosis, remains a major global health challenge. Nucleomodulins, bacterial effectors that target the host cell nuclei, are increasingly recognized as key virulence factors, but their roles in mycobacterial pathogenesis remain incompletely elucidated. Here, we characterize a hypothetical protein Rv2577 (designated MmpE) not only as a Fe^{3+}/Zn^{2+}-dependent metallophosphatase but also as a critical nucleomodulin involved in immune evasion and intracellular persistence. MmpE utilizes two nuclear localization signals, $RRR^{20–22}$ and $RRK^{460–462}$, to enter the host cell nucleus, where it binds to the promoter region of the vitamin D receptor (VDR) gene, thereby inhibiting host inflammatory gene expression. Additionally, MmpE represses the PI3K–Akt–mTOR signaling pathway, which arrests phagosome maturation. These actions collectively facilitate immune suppression and promote mycobacterial survival in macrophages and in mice. Our findings identify MmpE as a conserved nucleomodulin in mycobacteria and reveal a novel mechanism of MmpE-mediated intracellular survival.

Keywords Mycobacterium; Nucleomodulin; Metallophosphatase; Immune evasion; Intracellular survival.

Introduction

Mycobacterium tuberculosis (Mtb), the etiological agent of tuberculosis, has posed a persistent global health burden for centuries. Despite significant advances in elucidating the molecular mechanisms of its pathogenesis, current research has largely focused on effector proteins that modulate host cell membrane and cytoplasmic processes (Nisa *et al.,* 2022; Nasiri and Venketaraman, 2025). In contrast, investigations into effector proteins that target the host cell nucleus, the central hub for gene regulation and cellular control, remain comparatively limited.

Nucleomodulins are a class of bacterial effector proteins that can translocate into the host nucleus, where they modulate nuclear processes to promote pathogen survival (Chai *et al.,* 2020; Bierne and Cossart, 2021). These proteins affect host gene

29 expression by directly interacting with chromatin or by mimicking transcription factors,
30 chromatin modifiers, or other nuclear regulators (Li *et al.,* 2013; Rolando *et al.,* 2013;
31 Mitra *et al.,* 2018; Hanford *et al.,* 2021). For instance, LntA from *Listeria*
32 *monocytogenes* directly binds the chromatin repressor BAHD1, disrupting its function
33 and derepressing interferon-stimulated genes in a type III interferon-dependent
34 manner, ultimately promoting bacterial persistence (Lebreton *et al.,* 2011; Lebreton *et*
35 *al.,* 2014). Similarly, Ank1 and Ank6 from *Orientia tsutsugamushi* localize to the host
36 nucleus and facilitate the export of the NF-κB p65 subunit via exportin 1, thereby
37 suppressing the transcription of pro-inflammatory genes (Evans *et al.,* 2018; Steiert
38 and Weber, 2025). Although bacterial nucleomodulins utilize diverse strategies to
39 manipulate host nuclear functions, the identity and functional characterization of *M.*
40 *tuberculosis* nucleomodulins remain poorly defined.

41 Nucleomodulins employ various strategies to enter access to the host cell nucleus,
42 including passive diffusion, hijacking host proteins that contain nuclear localization
43 signals (NLSs), or using of their own NLSs to interact with the nuclear pore complex
44 (Hanford *et al.,* 2021). Among these mechanisms, NLSs play a particularly important
45 role. Based on their amino acid composition, NLSs are broadly classified into classical
46 (cNLS), non-classical (ncNLS), and other types (Lange *et al.,* 2008; Lu *et al.,* 2021).
47 Classical NLSs are further divided into monopartite (MP) and bipartite (BP) forms.
48 Monopartite NLSs consist of a single cluster of 4–8 basic residues, primarily lysine (K)
49 or arginine (R), with a typical consensus motif of K-K/R-X-K/R (Fontes *et al.,* 2000;
50 Kosugi *et al.,* 2009; Cautain *et al.,* 2015). Nuclear localization enables these effectors
51 to manipulate host gene expression, disrupt immune signaling, and reprogram cellular
52 processes to promote pathogen survival. For example, EspF from enteropathogenic
53 *Escherichia coli* contains an N-terminal NLS that directs it to the nucleolus, where it
54 interferes with ribosome biogenesis (Dean *et al.,* 2010; Singh *et al.,* 2018). NUE, a
55 SET domain-containing nucleomodulin secreted by *Chlamydia trachomatis*, also
56 possesses an NLS that mediates its nuclear localization, where it functions as a
57 histone lysine methyltransferase (HKMTase) targeting host histones H2B, H3, and H4

(Pennini *et al.,* 2010; Jermy, 2010).

Beyond their nuclear localization capabilities, some nucleomodulins directly affect host immunity through intrinsic enzymatic activities (Agarwal *et al.,* 2012). For example, the nucleomodulin PtpA promotes Mtb survival within macrophages by dephosphorylating host cytoplasmic proteins (Wang *et al.,* 2017). NleC from *E. coli*, a Zn-dependent metalloprotease, suppresses host immune responses by cleaving the p65 subunit of NF-κB in the cytoplasm, thereby inhibiting its nuclear translocation, and can enter the nucleus to reduce nuclear p65 levels, blocking NF-κB-dependent transcription of pro-inflammatory genes (Baruch *et al.,* 2011; Hodgson *et al.,* 2015). Among these enzymatically active nucleomodulins, purple acid phosphatases (PAPs) represent a distinct and functionally significant, yet underexplored, subclass within the metallophosphatase superfamily. PAPs are characterized by a conserved β-α-β-α-β fold and five signature motifs (DxG, GDXXY, GNH[D/E], VXXH, GHXH), which coordinate seven metal-ligating residues at a binuclear metal center (Rodriguez *et al.,* 2014; Bhadouria *et al.,* 2017; Bhadouria and Giri, 2022). These enzymes have been extensively studied in plants and mammals, where they are involved in key biological processes such as phosphorus metabolism and the generation of reactive oxygen species (Comba *et al.,* 2013; Feder *et al.,* 2020; Liu *et al.,* 2025). In contrast, only a few bacterial PAPs have been identified, such as BcPAP from *Burkholderia cenocepacia*, and their functions remain largely unknown (Yeung *et al.,* 2009). Notably, in Mtb, MmpE is the only identified PAP protein (Schenk *et al.,* 2000), but its specific contribution to infection and pathogenesis remain elusive.

In this study, we characterized MmpE as a conserved nucleomodulin in mycobacteria and demonstrated its nuclear translocation mediated by two NLSs, $RRR^{20–22}$ and $RRK^{460–462}$. Upon entering the nuclear, MmpE binds to the promoter region of the VDR gene, a key regulator of antimicrobial responses, resulting in transcriptional repression of pro-inflammatory genes. In addition, MmpE inhibits phagosome maturation by suppressing the expression of genes in the PI3K–Akt–mTOR signaling pathway. These actions collectively facilitate increased intracellular survival in both macrophage and

87 mouse. Beyond its nuclear function, MmpE functions as a Fe^{3+}/Zn^{2+}
88 metallophosphatase, with enzymatic activity reliant on the conserved residues His^{348}
89 and Asp^{359}, and partially contributes to intracellular survival. Taken together, our
90 findings identify MmpE as a bifunctional effector that integrates immune modulation
91 and enzymatic catalysis, underscoring its role in mycobacterial pathogenesis and its
92 potential as a therapeutic target.

93 **Results**

94 **NLSs are required for the nuclear translocation of MmpE**

95 In the prior study, we systematically identified some conserved nucleomodulins in
96 mycobacterium. Among them, the hypothetical protein Rv2577 (MmpE) was identified
97 as a candidate exhibiting strong nuclear localization in mammalian cells (Chen *et al.,*
98 2025). Based on these findings, we transfected HEK293T cells with a C-terminal
99 EGFP-tagged MmpE (MmpE-EGFP) and monitored its transcriptional level and
100 nuclear localization at different time points. As a result, a time-dependent increase in
101 the MmpE-EGFP content was observed in the host nucleus (Figure 1A, upper panel;
102 Figure S1A). Nuclear–cytoplasmic fractionation assays further confirmed these results,
103 showing a progressive enrichment of MmpE in the nuclear compartment over the
104 course of transfection (Figure 1A, bottom panel). Collectively, these results indicate
105 that MmpE possesses intrinsic nuclear translocation ability.

106 MmpE contains two putative NLSs, N-terminus ($RRR^{20–22}$, NLS1) and C-terminus
107 ($RRK^{460-462}$, NLS2) (Figure 1B). To evaluate the structural contribution of these motifs,
108 we utilized AlphaFold to model the impact of NLS truncations on the overall
109 conformation of MmpE. The predicted structures indicated that deletion of either NLS1,
110 NLS2, or both did not obviously alter the the protein fold (Figure S1B). Based on this
111 analysis, we generated a series of NLS-deleted mutants, including $MmpE^{\Delta NLS1}$,
112 $MmpE^{\Delta NLS2}$, and $MmpE^{\Delta NLS1-2}$, to assess the functional relevance of each motif in
113 nuclear localization. Subcellular localization of wild-type MmpE-EGFP and NLS
114 deletion mutants was examined in HEK293T cells by fluorescence microscopy at 36

115 hpt (hours post-transfection). Deletion of either NLS1 or NLS2 alone significantly
116 reduced the nuclear accumulation of MmpE-EGFP, with the effect of NLS2 deletion
117 being more pronounced than that of NLS1. Simultaneous deletion of both NLS motifs
118 ($MmpE^{\Delta NLS1\text{-}2}$) completely abolished nuclear localization, resulting in exclusive
119 cytoplasmic distribution (Figure 1C and D). These findings were further validated by
120 immunoblotting of nuclear and cytoplasmic fractions. Under the similar transfection
121 conditions, wild-type MmpE-EGFP was detected in both compartments, whereas
122 $MmpE^{\Delta NLS1}$ and $MmpE^{\Delta NLS2}$ exhibited substantially reduced nuclear abundance. By
123 contrast, $MmpE^{\Delta NLS1\text{-}2}$ was exclusively localized to the cytoplasmic fraction, suggesting
124 that both NLS motifs are required for efficient nuclear import (Figure 1E). Taken
125 together, our findings identify MmpE as a nucleomodulin, with nuclear import mediated
126 by the N- and C-terminal NLS motifs.

127 **Deletion of NLSs does not alter the phosphatase activity of MmpE**

128 Bioinformatic analyses identified MmpE as a Fe^{3+}/Zn^{2+}-metallophosphatase containing
129 a purple acid phosphatase (PAP) motif (Figure 2A; Figure S2A). Multiple sequence
130 alignment and phylogenetic reconstruction revealed that MmpE is highly conserved
131 among mycobacterial species and harbors canonical motifs characteristic of
132 metallophosphatases, including GD, GNHX, and GHXH (Figure 2B, Figure S2B).
133 These motifs are typically associated with enzymes that catalyze phosphate hydrolysis
134 via a binuclear metal ion-dependent mechanism, wherein residues such as Asp, His,
135 and Asn coordinate essential metal cofactors, commonly Fe^{3+}, Mn^{2+}, or Zn^{2+}, at the
136 active site.

137 To identify key amino acid residues of MmpE involved in metal coordination, AlphaFold
138 was used to predict the structure of MmpE, followed by the molecular docking using
139 PyMOL. As shown in Figure 2C, H^{348} and N^{359} were identified as candidate residues
140 likely involved in metal ion coordination within the predicted active site. Subsequently,
141 recombinant MBP-tagged MmpE deleting the Tat signal peptide ($MmpE^{\Delta Tat}$) was
142 subjected to *in vitro* phosphatase assays using *p*-nitrophenyl phosphate (*p*-NPP) as
143 the substrate. Reactions were supplemented with varying concentrations of Fe^{3+} and

144 Zn^{2+} to evaluate their individual effects on MmpE enzymatic activity. The results
145 demonstrated that, at equivalent concentrations, Fe^{3+} significantly enhanced MmpE
146 activity compared to Zn^{2+}, with maximal enzymatic activity was observed at 50 μM Fe^{3+}
147 (Figure 2D). Next, a double mutant ($MmpE^{\Delta Tat}$-$H^{348}AN^{359}A$) was generated via site-
148 directed mutagenesis to validate the functional importance of these residues. As
149 shown in Figure 2E, the addition of 50 μM Fe^{3+} significantly increased the *in vitro*
150 phosphatase activity of $MmpE^{\Delta Tat}$ compared to reactions without metal ions. However,
151 the enzymatic activity of the $MmpE^{\Delta Tat}$-$H^{348}AN^{359}A$ in the presence of 50 μM Fe^{3+} was
152 markedly reduced and nearly indistinguishable from that of $MmpE^{\Delta Tat}$ under metal-free
153 conditions. These results confirm that residues H^{348} and N^{359} are essential for Fe^{3+}
154 binding and catalytic activity.

155 Given that MmpE relies on NLSs to enter the host nucleus, we examined whether
156 deletion of NLS affects its phosphatase activity. Compared to wild-type MmpE, the
157 NLS-deleted mutant showed no significant change in enzymatic activity (Figure 2F),
158 which is consistent with the structural comparison results (Figure S1B). Collectively,
159 these results suggest that MmpE is a highly conserved Fe^{3+}/Zn^{2+}-dependent
160 metallophosphatase in mycobacteria, and its enzymatic activity is independent of NLS.

161 **The nuclear translocation and phosphatase activity of MmpE are essential for *M.***
162 ***bovis* BCG survival in macrophage cells**

163 To investigate the role of MmpE during infection, we first generated recombinant *M.*
164 *bovis* BCG strains expressing C-terminally Flag-tagged Ag85B (positive control) and
165 MmpE. Immunoblot analysis confirmed high levels of Ag85B-2×Flag and MmpE-
166 2×Flag in bacterial lysates, and both proteins were also detected in the culture
167 supernatants (Figure S3A), indicating that MmpE is indeed a secreted protein.

168 Furthermore, a series of recombinant BCG strains were constructed, including wild-
169 type (WT), *mmpE*-deleted mutant (ΔMmpE) (Figure S3B), ΔMmpE complemented with
170 wild-type *mmpE* (Comp-MmpE), and ΔMmpE complemented with NLS-deleted mutant
171 (Comp-$MmpE^{\Delta NLS1}$, Comp-$MmpE^{\Delta NLS2}$, and Comp-$MmpE^{\Delta NLS1\text{-}2}$). Deletion of NLS1

172 may reduce or abolish MmpE secretion (Stanley *et al.,* 2000; Buchanan *et al.,* 2001),
173 while deletion of NLS2 impaired its nuclear localization. All strains exhibited similar
174 growth rate under the normal culture conditions (Figure S3C). Subsequently, these
175 strains were used to infect THP-1 macrophages. As shown in Figure 3A and B, the
176 bacterial load of the ΔMmpE strain exhibited significantly reduced relative to the WT
177 strain, and bacterial clearance was accelerated over time. The phenotype of ΔMmpE
178 was rescued by complementation with wild-type gene *mmpE*. Meanwhile, the load of
179 the Comp-MmpE$^{\Delta NLS2}$ strain displayed significantly lower compared to Comp-MmpE in
180 both THP-1 and RAW264.7 macrophages, indicating that nuclear localization mediated
181 by NLS2 is critical for MmpE function. Notably, the Comp-MmpE$^{\Delta NLS1}$ and Comp-
182 MmpE$^{\Delta NLS1\text{-}2}$ strains demonstrated obvious higher load than those of the ΔMmpE strain,
183 yet lower than those of the Comp-MmpE strain (Figure 3C and D). These results
184 suggest that MmpE contributes to virulence not only through nuclear modulation but
185 also through additional mechanisms.

186 Next, we investigated the role of the Fe^{3+}/Zn^{2+}-dependent metallophosphatase of
187 MmpE on intracellular survival. As shown in Figure S3D, a double mutant strain (Comp-
188 MmpE-$H^{348}AN^{359}A$) was constructed and used to infect macrophage cells. The results
189 showed that this mutant exhibited significantly reduced intracellular load compared
190 with the Comp-MmpE strain (Figure 3E), indicating that the phosphatase activity also
191 plays an essential role in MmpE-mediated bacterial survival. To reveal the underlying
192 mechanism, cytokine expression assays were conducted in infected macrophages.
193 Compared with the WT and Comp-MmpE strains, cells infected with the ΔMmpE and
194 Comp-MmpE$^{\Delta NLS1\text{-}2}$ strains showed markedly elevated levels of pro-inflammatory
195 cytokines, including *IL1A*, *IL1B*, and *IL6* (Figure 3F).

196 Collectively, these results suggest that MmpE functions as a bifunctional effector,
197 possessing both nuclear import capability and phosphatase activity, promoting immune
198 evasion and enhancing intracellular survival during infection.

199 **MmpE modulates host transcription network involved in inflammation response**
200 **and lysosomal maturation**

201 To investigate the role of the nucleomodulin MmpE on host gene expression, we
202 performed RNA-seq assays on THP-1 macrophages infected with either wild-type
203 (BCG/wt) or MmpE-deleted (Ko*mmpE*) strains at 20 hpi (hours post-infection). As a
204 result, a total of 175 differentially expressed genes (DEGs) were identified, with 142
205 genes upregulated and 33 genes downregulated in Ko*mmpE*-infected macrophages
206 compared to those infected with BCG/wt (Figure 4A, Table S1). These DEGs were
207 significantly enriched in immune-related biological processes, particularly those
208 associated with apoptosis and cell death, as well as molecular functions related to
209 immune activation and cellular stress responses, such as pyrophosphatase activity
210 and nucleoside-triphosphatase activity (Figure 4B). Further analysis using the Kyoto
211 Encyclopedia of Genes and Genomes (KEGG) revealed that the DEGs were primarily
212 involved in immune and inflammatory signaling pathways, including cytokine–cytokine
213 receptor interaction, TNF signaling, Toll-like receptor signaling, chemokine signaling,
214 NF-κB signaling, JAK–STAT signaling, and the PI3K−Akt signaling pathway.
215 Additionally, several DEGs were enriched in pathways related to cell survival and
216 apoptosis. Another group of DEGs was associated with host defense mechanisms, as
217 evidenced by their enrichment in the lysosome pathway (Figure 4C). Together, these
218 data highlight MmpE as a critical modulator of host transcriptional responses that
219 facilitate mycobacterial immune evasion and intracellular survival.

220 To gain further insight into the functional relevance of the 175 differentially expressed
221 genes, we performed protein–protein interaction (PPI) network analysis, focusing on
222 protein-coding genes, which accounted for 38% of the total (Figure S4A). A tightly
223 connected network centered around key immune regulatory, including IL23A, IL12B,
224 CSF2, CD69, IDO1, and CEACAM1, which are critically involved in inflammatory
225 cytokine production (Figure 4D). Consistently, these genes expression was
226 upregulation in Ko*mmpE*-infected macrophages (Figure 4E). Given that inflammatory
227 signaling and lysosomal function are both essential for macrophage-mediated host
228 defense against mycobacterial infection, we further examined the expression of
229 representative inflammatory cytokines and key lysosomal maturation markers under

230 the same experimental conditions, such as *TFEB*, *LAMP1*, *LAMP2*, and several V-
231 ATPase subunit genes (*ATP6V0A1*, *ATP6V0C*, *ATP6V1A*, *ATP6V1B2*, and
232 *ATP6V1E1*). Consistent with transcriptomic findings, the Ko*mmpE* strain induced
233 significantly higher expression of both inflammatory cytokines and lysosomal
234 maturation-related genes compared to the WT strain (Figure 4F and G). Both the
235 Comp-MmpE$^{\Delta NLS2}$ and Comp-MmpE$^{\Delta NLS1\text{-}2}$ strains showed significantly higher
236 expression of these cytokine genes compared to the Comp-MmpE strain (Figure S4B
237 and C). Taken together, these results suggest that MmpE manipulates host
238 transcriptional networks governing inflammation and lysosomal function, thereby
239 subverting antimicrobial immunity.

240 **MmpE suppresses the expression of *VDR* and inhibits activation of the PI3K–**
241 **Akt–mTOR signaling pathway**

242 To elucidate the mechanism by which MmpE modulates host gene expression, we
243 performed ChIP-seq in HEK293T cells transfected with EGFP-MmpE. 2,903 potential
244 MmpE-binding sites (Table S2) were identified, with 18.49% (537) in intergenic regions
245 and 39.44% (1145) in intragenic regions (Figure 5A). Chromosomal distribution
246 revealed significant enrichment on chromosomes 1 and 2 (Figure 5B). Notably, 99.7%
247 (2894) of these binding sites were associated with protein-coding regions. Among
248 these, 1013 sites were located within 3 kb of transcription start sites (TSS), including
249 promoter (≤1 kb, 63.18%), promoter (1–2 kb, 22.9%), and promoter (2–3 kb, 13.92%)
250 (Figure 5C and D), suggesting that MmpE primarily targets promoter regions to
251 regulate transcription. PPI analysis of the 1013 potential target genes revealed
252 significant enrichment in protein kinase-related genes, such as *PRKCB*, *PLCG2* and
253 *PIK3CB*, involved in regulating immune activation and inflammatory responses via the
254 PI3K–Akt and mTOR signaling pathways, suggesting that MmpE may influence cell
255 immune responses through a coordinated network of signaling pathways (Figure S5A
256 and B). In parallel, we examined the expression of key components in this signaling
257 axis in THP-1 macrophages infected with either BCG/wt or the Ko*mmpE* strains.
258 Notably, Ko*mmpE* infection led to a significant upregulation of genes associated with

259 the pathway, including *PIK3CA*, *PIK3CB*, *PIK3R1*, *mTOR*, *AKT1–3*, and *FOXO1/3*
260 (Figure S5C). These genes encode critical regulators of cell survival and immune
261 activation within the PI3K–Akt–mTOR axis.

262 To identify the direct target gene of MmpE in macrophages, we focused on analysis of
263 the promoter regions (≤1 kb upstream of the transcription start site) of significantly
264 upregulated genes with | $Log_2FC > 1$| and $P < 0.05$. Four transcription factors were
265 identified, including CREBBP, VDR, GREB1, and FOXP4 (Figure 5E). Integrative
266 analysis using HOMER *de novo* motif prediction revealed that only the promoter region
267 of *VDR*, a key anti-inflammatory gene (Aggeletopoulou *et al.,* 2022), harbored a
268 potential MmpE-binding motif (Figure 5F). These findings suggest that MmpE may
269 directly bind to the *VDR* promoter. To validate the hypothesis, we examined *VDR*
270 expression in macrophages infected with recombinant strains. Compared to the
271 BCG/wt, *VDR* expression was significantly downregulated in THP-1 cells infected with
272 the Ko*mmpE* strain (Figure S5D). To further test whether MmpE directly binds the *VDR*
273 promoter, we cloned the *VDR* promoter region (−100 bp to +50 bp) and performed
274 chromatin immunoprecipitation (ChIP) assays in HEK293T cells. While both *VDR* and
275 *GAPDH* (control) sequences were present in input samples, *VDR* promoter DNA was
276 detected exclusively in ChIP samples from EGFP-MmpE transfected cells (Figure 5G
277 and H). Furthermore, the DNA-binding capacity of MmpE was unaffected by its
278 phosphatase activity (Figure S5E and F). To confirm these results, we performed
279 electrophoretic mobility shift assays (EMSA) using the same *VDR* promoter fragment.
280 As shown in Figure 5I and 5J, the shift bands corresponding to MmpE and *VDR*
281 promoter complex were observed, and a corresponding increase was observed in the
282 percentage of protein/DNA complexes. Collectively, these results provide strong
283 evidence that MmpE directly interacts with the *VDR* promoter both in vivo and *in vitro*
284 to repress host inflammatory signaling pathways and facilitating immune evasion
285 during mycobacterial infection.

286 To further characterize the transcriptional programs regulated by MmpE, we performed
287 an integrative analysis of CUT&Tag and RNA-seq datasets. This analysis identified

298 DEGs with direct or proximal MmpE binding sites (Table S3; Figure S6A and B). Notably, genes such as *RHEX*, *PLXDC1*, and *GAS6* exhibited significant expression changes and were enriched in pathways associated with cell differentiation and small GTPase-mediated signaling (Figure S6C and D). These pathways play critical roles in shaping immune cell function, trafficking, and inflammatory responses during host–pathogen interactions (Li *et al.,* 2023; Ma *et al.,* 2024). Taken together, these data establish MmpE as a nucleomodulin that directly alters host transcriptional networks involved in immune regulation and cellular defense, thereby supporting mycobacterial survival within host cells.

Nuclear translocation of MmpE is essential for mycobacterial survival in mice

Next, C57BL/6 mice were intranasally infected with *M. bovis* BCG strains, including wild-type (WT), ΔMmpE, Comp-MmpE, and Comp-MmpE$^{\Delta NLS1\text{-}2}$, and systematically assessed bacterial persistence, pulmonary inflammation, and cytokine dynamics. Our results show that mice infected with the ΔMmpE strain exhibited significantly lower bacterial loads in the infected mice lung compared to those infected with the WT or Comp-MmpE strains. Remarkably, mice infected with the Comp-MmpE$^{\Delta NLS1\text{-}2}$ strain showed significantly lower than those in the Comp-MmpE strains but higher than those in the ΔMmpE strains (Figure 6A). A similar trend was observed in splenic bacterial colonization (Figure S7). Hematoxylin and eosin (H&E) staining revealed extensive inflammatory infiltrates in the lungs of mice infected with WT or Comp-MmpE, whereas mice infected with ΔMmpE or Comp-MmpE$^{\Delta NLS1\text{-}2}$ exhibited markedly reduced inflammation (Figure 6B). Mice infected with ΔMmpE and Comp-MmpE$^{\Delta NLS1\text{-}2}$ strains exhibited significantly elevated levels of *Il1α*, *Il1β*, and *Il6* compared to those infected with WT or Comp-MmpE strains, despite lower bacterial burdens (Figure 6C and E).

Collectively, these results demonstrate that MmpE indeed contributes to *M. bovis* BCG survival *in vivo*, with its nuclear translocation being essential for mycobacterial intracellular survival.

Discussion

316 **MmpE Functions as a Bifunctional Protein with Nuclear Localization and**
317 **Phosphatase Activity.** In this study, we identified two independent NLSs within the
318 MmpE protein, $RRR^{20–22}$ (NLS1) and $RRK^{460–462}$ (NLS2), which together form a bipartite
319 NLS motif that is rarely observed in bacterial effector proteins. Loss of a single NLS
320 significantly reduced the nuclear accumulation of MmpE, with NLS2 deletion causing
321 a more pronounced effect than that of NLS1. Simultaneous deletion of both motifs
322 completely abolished nuclear localization (Figure 1C-E). These findings indicate that
323 NLS1 and NLS2 function in a synergistic manner, with NLS2 likely playing a dominant
324 role in nuclear import. Further sequence analysis revealed that NLS1 ($RRR^{20–22}$) is
325 embedded within the conserved twin-arginine translocation (Tat) signal motif (S/TRR-
326 X-FLK), a well-characterized determinant of Tat-dependent secretion (Gimenez *et al.,*
327 2018). The adjacent twin-arginine residues are critical for recognition by the Tat
328 translocase, and mutations in this motif have been shown to significantly impair or
329 abolish secretion (Ulfig *et al.,* 2017). Accordingly, the Comp-$MmpE^{\Delta NLS1}$ strain likely
330 exhibits impaired secretion, and the Comp-$MmpE^{\Delta NLS2}$ strain is deficient in nuclear
331 localization. Consistent with this, both the Comp-$MmpE^{\Delta NLS1}$ and Comp-$MmpE^{\Delta NLS2}$
332 strains exhibited lower intracellular survival than the Comp-MmpE strain and higher
333 than that of the ΔMmpE strain (Figure 3A-D), suggesting that the nuclear localization
334 ability of MmpE indeed contributes to bacterial survival. Interestingly, MmpE also
335 functions as a Fe^{3+}/Zn^{2+}-dependent metallophosphatase, with residues H^{348} and N^{359}
336 being essential for its catalytic activity (Figure 2D and E). The mutant strain (Comp-
337 MmpE-$H^{348}AN^{359}A$) showed markedly reduced intracellular survival Compared to
338 Comp-MmpE (Figure 3E), indicating that the phosphatase activity of MmpE is also
339 required for intracellular survival. This explains why the intracellular survival of the
340 Comp-$MmpE^{\Delta NLS1-2}$ strain is significantly lower than that of the Comp-MmpE strain, yet
341 obviously higher than that of the ΔMmpE strain (Figure 3C and D, Figure 6A).

342 Taken together, these findings suggest that MmpE is a dual-function effector protein
343 that promotes intracellular survival during infection through the coordinated action of
344 its nuclear localization signal and phosphatase activity.

345 **MmpE's direct targeting of the host gene *VDR* represents a unique immune**
346 **evasion strategy.** VDR is a critical nuclear receptor that controls the expression of
347 numerous genes involved in host immune defense, including antimicrobial peptides
348 and cytokines (Usategui-Martín *et al.,* 2022). For example, Mtb suppresses the
349 expression of the host gene *CYP27B1* to reduce active vitamin D synthesis, thereby
350 limiting VDR activation and downstream antimicrobial responses (Liu *et al.,* 2006).
351 Similarly, *Salmonella* downregulates *VDR* through miRNA-mediated mechanisms,
352 weakening mucosal immunity (Chen *et al.,* 2014). In this study, we found that MmpE
353 directly binds to the promoter of the *VDR* gene (Figure 5F–J) and attenuates the
354 expression of VDR-regulated inflammatory genes (Figure 3F; Figure 6C-E), ultimately
355 promoting bacterial intracellular survival (Figure 6A). This mode of action represents a
356 novel strategy employed by bacterial pathogens to evade host defenses through the
357 direct manipulation of host gene promoters by nucleomodulins. Although previous
358 studies have reported that bacterial nucleomodulins interfere with the host
359 transcriptional machinery, these effects have typically occurred indirectly, such as
360 through epigenetic modifications or inhibition of signaling pathways (Jose *et al.,* 2016;
361 Singh *et al.,* 2023). Direct promoter binding by a nucleomodulin, however, remains
362 relatively uncommon and represents a distinct mechanism of host gene regulation.

363 **MmpE regulates the expression of host genes involved in phagosome**
364 **maturation.** As an intracellular pathogen, Mtb employs multiple strategies to evade
365 phagolysosomal degradation, a process essential for bacterial clearance (Chandra *et*
366 *al.,* 2022; Zhang *et al.,* 2023; Singh and Nagaraja, 2025). Improtantly, approximately
367 70% of phagosomes harboring Mtb fail to fuse with lysosomes, in part due to the
368 activity of secreted phosphatases such as PtpA, PknG, and SapM, which disrupt
369 vesicular trafficking (Wong *et al.,* 2011; Ge *et al.,* 2022; Zhang *et al.,* 2024; Alsayed
370 and Gunosewoyo, 2024). MmpE has also been shown to contribute to the arrest of
371 phagosome maturation in human cells, although the underlying mechanisms remain
372 unclear (Forrellad *et al.,* 2020). In this study, we identify a potential mechanism by
373 which MmpE inhibits phagosome maturation. Deletion of *mmpE* led to significant

374 upregulation of lysosome-associated genes, including *TFEB*, *LAMP1*, *LAMP2*, and V-
375 ATPase subunit genes (Figure 4C and G). Among these, TFEB is a master
376 transcriptional regulator of lysosomal biogenesis and function (Jeong *et al.,* 2021;
377 Wang *et al.,* 2024). Furthermore, ChIP-seq analysis revealed that MmpE directly binds
378 to promoter regions of host genes within the PI3K–Akt–mTOR signaling pathway
379 (Figure S5A), a key upstream regulator of TFEB activity (Fang *et al.,* 2021; Gounis *et*
380 *al.,* 2025). Collectively, these results indicate that MmpE may act as a transcriptional
381 regulator that targets the PI3K–Akt–mTOR–TFEB axis, thereby inhibiting lysosomal
382 maturation.

383 **MmpE is a Fe^{3+}/Zn^{2+}-dependent metallophosphatase that is essential for**
384 **mycobacterial intracellular survival.** Previous studies have shown that
385 phosphatases play critical roles in host–pathogen interactions by modulating
386 phosphorylation-dependent signaling pathways (Sajid *et al.,* 2015; Bonne Køhler *et al.,*
387 2020). In bacterial pathogens, these enzymes frequently contribute to immune evasion
388 and intracellular survival. For example, the tyrosine phosphatase YopH from *Yersinia*
389 *enterocolitica* disrupts phagocytic signaling in host macrophages, thereby impairing
390 oxidative burst responses and promoting bacterial persistence (Davicino *et al.,* 2017;
391 Shaban *et al.,* 2020). Similarly, PpzA, a phosphatase from *Aspergillus fumigatus*, has
392 been implicated in fungal adaptation to immune pressure under iron-replete conditions
393 (Manfiolli *et al.,* 2017; Kurucz *et al.,* 2018). In this study, we found that MmpE contains
394 a predicted purple acid phosphatase (PAP)-like domain and exhibits phosphatase
395 activity that requires Fe^{3+} and Zn^{2+} ions as cofactors (Figure 2A and D). Through site-
396 directed mutagenesis, we identified His^{348} and Asn^{359} as critical residues for Fe^{3+}
397 coordination. Substitution of these residues ($H^{348}AN^{359}A$) significantly impaired
398 phosphatase function in the presence of Fe^{3+}, leading to a marked reduction in
399 bacterial intracellular load (Figure 2E; Figure 3E). However, the precise molecular
400 mechanism by which MmpE interacts with Fe^{3+} remains to be elucidated in future
401 studies.

402 In conclusion, our study identifies MmpE as a novel bifunctional virulence factor of

403 mycobacteria, combining Fe^{3+}/Zn^{2+}-dependent phosphatase activity with nuclear
404 translocation capability. MmpE translocates into the host nucleus and directly binds to
405 the promoters of some key host genes, such as *VDR*, thereby inhibiting the expression
406 of the downstream targets implicated with the inflammation responses and lysosomal
407 maturation, thereby promoting mycobacterial survival in macrophages and in mice
408 (Figure 7). These findings reveal a sophisticated mechanism by which bacterial
409 pathogen manipulates host gene transcription and signaling pathway to promote
410 intracellular persistence.

411 **Materials and methods**

412 **Key resources used in this study**

Reagent or resource	Source	Identifier
Antibodies		
Anti-β-actin	Abbkine	Cat#ABL1010
Anti-Histone H3	Abbkine	Cat#ABL1070
Goat anti-rabbit IgG	Abbkine	Cat#A21020
Goat anti-mouse IgG	Abbkine	Cat#A25012
Anti-GFP	Proteintech	Cat#66002-1-Ig
Anti-Flag	Proteintech	Cat#66008-4-Ig
Cell and Mouse		
HEK293T	ATCC	Cat#CRL-3216
RAW264.7	ATCC	Cat#TIB-71
THP-1	ATCC	Cat#TIB-202
Mouse (C57BL/6)	Chang-sheng Bio (Liaoning, China)	
The plasmids used in this study are listed in Table S4		
The bacterial strains used in this study are listed in Table S5		
The primers used in this study are listed in Table S6		
Chemicals, Peptides, and Recombinant Proteins		
DMEM	Gibco	Cat#11965092
RPMI 1640	Gibco	Cat#C11875500BT
Opti-MEM™	Gibco	Cat#31985070
FBS	Gibco	Cat#A5256701
Sodium pyruvate	Gibco	Cat#11360070
L-glutamine	Gibco	Cat#A2916801

Key Resources Used in This Study (Continued)		
Chemicals, Peptides, and Recombinant Proteins		
HEPES	Gibco	Cat#15630080
2-Mercaptoethanol	Gibco	Cat#21985023
penicillin-streptomycin antibiotics	Gibco	Cat#15140122
PMA	Sigma-Aldrich	Cat#P8139
p-NPP	Sigma-Aldrich	Cat#4264-83-9
Formaldehyde	Sigma-Aldrich	Cat#252549
OADC	MilliporeSigma	Cat#M0678
DAPI	Beyotime	Cat# P0126
Triton-X-100	Beyotime	Cat#P0096
RIPA buffer	Beyotime	Cat#P0038
NP-40	Beyotime	Cat#P0013F
protease inhibitor cocktail	Beyotime	Cat#AR1182
HieffTrans® Liposomal Transfection Reagent	YEASEN	Cat#40802ES03
protein A/G magnetic beads	MedChemExpress	Cat#HY-K0202
Critical commercial assays		
TRIpure Reagent	Aidlab	Cat#RN0101
EASYspin RNA Mini Kit	Aidlab	Cat#RN0702
EndoFreePlasmidMiniKit	Aidlab	Cat#PL0401
cDNA Reverse Transcription Kit	Vazyme	Cat#R333-01
2 × ChamQ Universal SYBR qPCR Master Mix	Vazyme	Cat#Q711-03
Uniclone One Step Seamless Cloning Kit	Genesand	Cat#SC612
Clarity™ Western ECL Substrate	BIO-RAD	Cat#1705060
Nuclear and Cytoplasmic Protein Extraction kit	Beyotime	Cat#P0027
Software and algorithms		
jvenn	https://bioinfogp.cnb.csic.es/tools/venny/index.html	
AlphaFold v2.2.0	https://github.com/deepmind/alphafold	
iTOL	https://itol.embl.de/	
ESPript 3.0	https://espript.ibcp.fr/ESPript/cgi-bin/ESPript.cgi	
GraphPad Prism 8	https://www.graphpad.com/	
UCSF Chimera	http://www.cgl.ucsf.edu/chimera/	
SignalP 5.0	https://services.healthtech.dtu.dk/services/SignalP-5.0/	

Key Resources Used in This Study (Continued)	
Software and algorithms	
MEGA 12.0	https://www.megasoftware.net/
STRING 12.0	https://cn.string-db.org/
Cytoscape 3.10.3	https://cytoscape.org/
CaseViewer version 2.0	https://www.3dhistech.com/solutions/caseviewer/

413 **Bacterial strains and culture conditions**

414 The bacterial strains used in this study are detailed in Table S5. *E. coli* DH5α and BL21
415 were cultured in Luria-Bertani (LB) medium under standard conditions. *M. bovis BCG*
416 strains were grown in Middlebrook 7H9 broth supplemented with 10% (v/v) OADC
417 (oleic acid, albumin, dextrose, catalase), 0.05% (v/v) Tween-80, and 2% (v/v) glycerol.
418 Antibiotics were added as required at the following final concentrations: 50 μg/mL
419 hygromycin (for mycobacteria) and 50 μg/mL kanamycin (for both mycobacteria and *E.*
420 *coli*).

421 **Cell culture**

422 THP-1 cells were cultured in Roswell Park memorial institute 1640 (RPMI 1640)
423 medium supplemented with 10% (v/v) heat-inactivated fetal bovine serum (FBS), 1 mM
424 sodium pyruvate, 2 mM L-glutamine, 10 mM HEPES buffer (pH 7.2–7.5), and 50 μM
425 2-mercaptoethanol. For differentiation into macrophages, THP-1 cells were treated
426 with 200 nM phorbol 12-myristate 13-acetate (PMA) for 24 h, followed by an additional
427 48 h incubation in fresh PMA-free medium to allow complete differentiation prior to
428 experimental use.

429 HEK293T and RAW264.7 monocytes were cultured in Dulbecco's modified Eagle's
430 medium (DMEM) supplemented with 10% (v/v) FBS and 50 μg/mL penicillin-
431 streptomycin. All cells were maintained at 37 °C in a humidified atmosphere with 5%
432 CO_2.

433 **Recombinant expression and secretion of MmpE**

434 Recombinant *M. bovis* BCG strains expressing C-terminally 2×Flag-tagged Ag85B
435 (positive control) and MmpE were constructed to assess protein expression and
436 secretion under standard *in vitro* culture conditions. The strains were cultured in

437 200 mL of Middlebrook 7H9 broth supplemented with 10% (v/v) OADC, 2% (v/v)
438 glycerol, and 0.05% Tween-80 at 37 °C until mid-log phase (OD_{600} = 0.6). Cultures
439 were centrifuged at 4,000 × g for 60 min to separate bacterial pellets from supernatants.
440 Pellets were washed and lysed by bead beating in phosphate-buffered saline (PBS)
441 supplemented with protease inhibitors. Culture supernatants were filtered through
442 0.22 μm sterile filters to remove residual bacteria and concentrated to a final volume
443 of 2 mL using Amicon Ultra centrifugal filters (10 kDa molecular weight cutoff). Both
444 bacterial lysates and concentrated supernatants were analyzed by SDS–PAGE
445 followed by immunoblotting using anti-Flag antibodies to detect the expression and
446 secretion of 2×Flag-tagged proteins.

447 **Phylogenetic and sequence analysis**

448 To investigate the evolutionary conservation and sequence features of MmpE
449 homologs, phylogenetic reconstruction was performed using MEGA version 12.0 and
450 iTOL platform with a neighbor-joining algorithm. Parameters included pairwise deletion
451 for gap treatment, a poisson substitution model (selected for its suitability in analyzing
452 closely related bacterial sequences), and 1,000 bootstrap replicates to assess node
453 support. Only nodes with bootstrap values ≥50% were retained, and no additional tree
454 pruning was applied.

455 The analysis combined metallophosphatase MmpE homologs from 11 *Mycobacterium*
456 strains, including *M. tuberculosis* (Mtu), *M. bovis* BCG (Mbb), *M. orygis* (Mory), *M.*
457 *kubicae* (Mku), *M. paraterrae* (Mpaa), *M. farcinogenes* (Mfg), *M. mucogenicum* (Mmuc),
458 *M. vicinigordonae* (Mgor), *M. lentiflavum* (Mlw), *M. avium* (Mav), *M. manitobense*
459 (Mman). Genomic sequences were retrieved from the NCBI RefSeq database, filtered
460 for completeness, and aligned using Clustal Omega v1.2.4 with default parameters
461 (gap opening penalty = 10, gap extension = 0.2, and iterative refinement enabled).
462 Sequence conservation was visualized using ESPript 3.0, with residues exhibiting ≥90%
463 identity across all homologs highlighted in red.

464 **Cell transfection and confocal microscopy**

465 HEK293T cells were seeded at 70% confluency in poly-L-lysine-coated 35-mm glass-

466 bottom dishes and maintained in DMEM supplemented with 10% (v/v) FBS at 37 °C
467 under 5% CO_2. Transfection was performed using the Hieff Trans™ Liposomal
468 Transfection Reagent according to the manufacturer's protocol. Briefly, 0.5 μg of
469 plasmid DNA and 1.5 μL of transfection reagent were diluted in 50 μL of Opti-MEM,
470 incubated at room temperature for 20 minutes, and then added dropwise to each well
471 of 35-mm six-chamber glass-bottom dishes.

472 At 24–48 hpt, cells were washed with PBS, fixed in 4% paraformaldehyde for 15 min,
473 and permeabilized with 0.1% Triton X-100 for 10 min. Nuclei were counterstained with
474 1 μg/mL DAPI (4′,6-diamidino-2-phenylindole) for 10 min. Confocal imaging was
475 performed using an Olympus FV1000 Confocal Laser Scanning Microscope equipped
476 with a 100×/1.40 NA oil immersion objective. EGFP and DAPI signals were detected
477 with 488 nm and 405 nm lasers, respectively. Spectral unmixing was carried out using
478 the Olympus FV10-ASW software (v4.2) to minimize signal cross-talk. Z-stack images
479 were acquired in sequential mode with a 0.5 μm step size across all samples to ensure
480 imaging consistency.

481 **Immunoblot analysis**

482 For immunoblotting, the cells were lysed in radioimmunoprecipitation assay (RIPA)
483 buffer supplemented with 1.5% (v/v) protease inhibitor cocktail. Protein concentrations
484 were quantified using the bicinchoninic acid (BCA) assay. Equal amounts of protein
485 (20–40 μg) were resolved by SDS-PAGE and transferred onto PVDF membranes.
486 Membranes were blocked for 1 h at room temperature with 5% (w/v) non-fat milk in
487 TBST (25 mM Tris, 150 mM NaCl, 2 mM KCl, and 0.2% Tween-20, pH 7.4) and
488 incubated overnight at 4 °C with primary antibodies. After three washes with TBST (10
489 min each), membranes were incubated with horseradish peroxidase (HRP)-conjugated
490 secondary antibodies for 1 hour at room temperature. Protein bands were visualized
491 using an enhanced chemiluminescence (ECL) substrate and imaged using the
492 ChemiDoc™ MP Imaging System (Bio-Rad). β-actin, GAPDH, or histone H3 was used
493 as an internal control for normalization. Antibody details are provided in the Key
494 resources table.

For subcellular fractionation, cytoplasmic and nuclear proteins were isolated using a Nuclear and Cytoplasmic Protein Extraction Kit (manufacturer's protocol). Briefly, after treatment, cells were washed and harvested in cold PBS. Cytoplasmic and nuclear fractions were separated according to the manufacturer's instructions. Protein concentrations were measured using the BCA assay, and equal amounts of protein were analyzed by immunoblotting as described above.

AlphaFold Predicted Structural Modeling of MmpE with NLS Truncations

The structural models of MmpE with NLS truncations were generated using AlphaFold version 2.2.0. The full-length MmpE sequence was used as the input to predict the reference structure. To assess the impact of NLS deletions, modified sequences were prepared by removing the residues corresponding to NLS1 ($RRR^{20–22}$), NLS2 ($RRK^{460–462}$), or both motifs. Structural prediction was performed for each sequence using the default AlphaFold parameters, which include the application of the pre-trained model and multiple sequence alignment (MSA) generation using the UniRef90 and MGnify databases. The confidence of the predictions was evaluated using the predicted local distance difference test (pLDDT) scores provided by AlphaFold. The resulting models were visualized and analyzed using UCSF ChimeraX to compare the overall protein conformations and assess structural changes due to NLS deletions.

Prediction of metal ion-binding residues in MmpE

The structure of MmpE was predicted using AlphaFold version 2.2.0 to investigate its potential metal ion dependence and identify key residues involved in metal coordination. The predicted structure was analyzed using PyMOL to identify residues within the putative active site. Residues were selected based on their spatial arrangement in the active site, and their proximity to regions likely involved in metal ion binding was annotated. Visualization and annotation of the predicted active site were performed using PyMOL to determine the potential roles of these residues in metal ion coordination.

Protein Expression and Purification

N-terminal maltose-binding protein (MBP)-tagged and C-terminal His_6-tagged wild-

524 type MmpE, as well as mutant variants lacking the Tat signal peptide were expressed
525 in *E. coli* BL21 (DE3). Protein expression was performed in 1 L of LB medium. Cultures
526 were grown at 37 °C until the optical density at 600 nm (OD_{600}) reached approximately
527 0.8, after which protein expression was induced with 0.2 mM isopropyl-β-D-
528 thiogalactopyranoside (IPTG) at 18 °C for 24 h. Following induction, cells were
529 harvested by centrifugation and lysed by sonication in ice-cold lysis buffer containing
530 150 mM NaCl, 30 mM Tris-HCl (pH 7.5), and 1 mM phenylmethylsulfonyl fluoride
531 (PMSF). The lysate was clarified by centrifugation, and the supernatant was subjected
532 to affinity purification using an MBP affinity column.

533 **Phosphatase activity assay**

534 Phosphatase activity was measured using *p*-nitrophenyl phosphate (*p*-NPP) as the
535 substrate in a final reaction volume of 200 μL. Reactions were initiated by incubating
536 0–80 μg of purified protein with *p*-NPP at 37 °C for 60 min. The release of *p*-nitrophenol
537 (*p*-NP), the dephosphorylated product, was quantified by measuring absorbance at
538 405 nm using a microplate spectrophotometer.

539 Kinetic parameters were determined under initial velocity (V_0) conditions using
540 substrate concentrations ranging from 0.1 to 10 mM *p*-NPP. The kinetic constants Km
541 and Vmax were calculated by fitting the data to the Michaelis-Menten equation using
542 nonlinear regression analysis in GraphPad Prism 8.0. The catalytic turnover rate (Kcat)
543 was calculated using the equation Kcat = $Vmax/E_0$, where Vmax was expressed as
544 ηM *p*-NP min^{-1} and E_0 represents the active enzyme concentration in ηM. Control
545 reactions were carried out in the absence of either the substrate or the enzyme to
546 measure background absorbance. All assays were performed in triplicate to ensure
547 the reproducibility of results.

548 **Quantitative real-time PCR**

549 THP-1 cells were infected with the *M. bovis* BCG strain and harvested 20 h post-
550 infection for total RNA isolation. RNA was extracted using 1 mL of TRIzol® reagent
551 following the manufacturer's protocol. To eliminate genomic DNA contamination, RNA
552 samples were treated with DNase I for 30 min at 37 °C, followed by heat inactivation

553 at 65 °C for 10 min. RNA concentration and purity were assessed using a NanoDrop
554 2000 spectrophotometer (Thermo Fisher Scientific).

555 For cDNA synthesis, 1 μg of total RNA was reverse transcribed using the HiScript® III
556 cDNA Reverse Transcription Kit with random hexamers primers, according to the
557 manufacturer's protocol. qRT-PCR was performed using ChamQ SYBR® Green RT-
558 PCR Master Mix. Relative mRNA expression levels were calculated using the $2^{-\Delta\Delta Ct}$
559 method, normalizing Ct values to the housekeeping gene *HPRT*. All qRT-PCR
560 experiments were conducted in triplicate, with at least three independent biological
561 replicates and two technical replicates per condition. Primer sequences are listed in
562 Table S6.

563 **RNA-seq analysis**

564 THP-1 cells were seeded at a density of 1×10^6 cells well in 6-well plates and
565 differentiated into macrophages by treatment with 100 nM PMA for 48 h. After
566 differentiation, cells were washed with PBS and infected with *M. bovis* BCG WT or
567 *KommpE* strains at a multiplicity of infection (MOI) of 10:1. Following 20 h of infection,
568 total RNA was extracted using TRIzol® reagent according to the manufacturer's
569 protocol.

570 High-quality sequencing reads were then aligned to the human reference genome
571 (GRCh38) using HISAT2 (v2.2.1). Transcript quantification was performed using
572 FeatureCounts (v2.0.3), and differential gene expression analysis was conducted
573 using DESeq2 (v1.38.3) in R. Genes with an adjusted *P*-value < 0.05 and an absolute
574 $|\log_2$ fold change ≥ 1| were considered significantly differentially expressed. RNA-seq
575 data were visualized using GraphPad Prism version 8.0, as well as volcano plots,
576 heatmaps, and other graphical outputs generated via the SRplot platform (Tang *et al.,*
577 2023).

578 **CUT&Tag analysis**

579 HEK293T cells were cultured in 10 cm^2 flat dish at a density of 1×10^7 cells per well
580 and transfected with 10 μg of the MmpE-pEGFP expression plasmid using Hieff

581 Trans™ Liposomal Transfection Reagent, following the manufacturer's protocol. Cells
582 transfected with the empty vector pEGFP-N1 served as controls. After 36 h of
583 transfection, cells were harvested for CUT&Tag analysis.

584 For the CUT&Tag, cells were cross-linked with 1% formaldehyde at room temperature
585 for 10 minutes, and the reaction was quenched with 0.125 M glycine. Cells were
586 collected by centrifugation and permeabilized using ice-cold wash buffer containing
587 0.05% digitonin. Primary antibody incubation was performed overnight at 4 °C using
588 mouse anti-GFP antibody (1:500 dilution), followed by a 2-hour incubation at room
589 temperature with a Protein A/G-conjugated secondary antibody (1:100 dilution). The
590 cells were then incubated at 37 °C for 1 hour with a Protein A–Tn5 transposase
591 complex (1:100 dilution) preloaded with Illumina sequencing adapters, enabling site-
592 specific cleavage and adapter insertion near MmpE binding sites.

593 The reaction was terminated using lysis buffer containing 10% SDS, followed by
594 proteinase K digestion. DNA was purified and amplified by PCR (12 cycles) using the
595 NEBNext Ultra II DNA Library Preparation Kit. Fragment size distribution (150–300 bp)
596 was confirmed using the Agilent 2100 Bioanalyzer.

597 Sequencing was performed on the Illumina NovaSeq 6000 platform, producing 150 bp
598 paired-end reads. Raw reads were quality-checked using FastQC and aligned to the
599 human reference genome (hg38). Peak calling was conducted using MACS2 (v2.2.7)
600 with the parameters --nomodel --qvalue 0.05, identifying 2,903 high-confidence MmpE
601 binding sites with >9-fold enrichment. Genomic annotation, including promoter
602 analysis and gene ontology (GO) enrichment, was performed using HOMER (v4.11).
603 *De novo* motif discovery was also conducted with HOMER, and motifs were statistically
604 validated using TOMTOM with a significance threshold of $P < 0.001$.

605 **Chromatin Immunoprecipitation (ChIP) assays**

606 ChIP assays were performed to validate the direct binding of MmpE to the promoter
607 regions of target genes. HEK293T cells were transfected with either an empty control
608 vector, EGFP, or MmpE–EGFP expression plasmids. Cross-linking, chromatin isolation,

609 fragmentation, and immunoprecipitation were carried out following the same procedure
610 described for the CUT&Tag experiments.

611 DNA was purified from both input and immunoprecipitated (IP) samples and subjected
612 to PCR using primers specific to the promoter regions of the target genes (–100 bp to
613 +50 bp relative to the transcription start site). *GAPDH* promoter primers were used as
614 a negative control. PCR products were analyzed by agarose gel electrophoresis to
615 assess the presence of enriched promoter fragments.

616 For quantitative analysis, ChIP–qPCR was performed to measure the enrichment of
617 specific promoter regions in IP samples. All reactions were carried out in triplicate.
618 Relative enrichment was calculated using the $2^{-\Delta Ct}$ method, normalized to input DNA.

619 **Electrophoretic mobility shift assays (EMSA)**

620 DNA substrates were amplified by PCR from the genomic DNA of *Mycobacterium*
621 *tuberculosis* H37Rv. The sequences of the oligonucleotide fragments used in the assay
622 are listed in Table S6. EMSA was carried out using a modified protocol as previously
623 described (Li *et al.,* 2020). Each 20 μL reaction contained PCR-amplified DNA
624 fragments, purified MmpE protein at varying concentrations, and binding buffer
625 composed of 50 mM Tris–HCl (pH 7.5), 50 mM NaCl, 50 mM $FeCl_3$, 0.05 mg/mL bovine
626 serum albumin (BSA), and 10% (v/v) glycerol. Reaction mixtures were incubated on
627 ice for 30 minutes to allow protein–DNA complex formation. Samples were then
628 resolved on a 4.8% native polyacrylamide gel using a running buffer containing 15 mM
629 Tris-HCl (pH 7.5) and 0.1 M glycine at 80 V. Following electrophoresis, gels were
630 stained with ethidium bromide and visualized using a Gel Imaging Analysis System
631 (JIAPENG, China).

632 **Colony-Forming Unit (CFU) assay**

633 For bacterial preparation, mid-log phase cultures of *M. bovis* BCG (OD_{600} = 0.8) were
634 harvested, washed with PBS, and resuspended in fresh medium. THP-1 cells were
635 seeded in 24-well plates at a density of 5×10^5 cells per well and infected at a MOI of
636 1:10. After 4 hours of infection, extracellular bacteria were removed by treatment with

637 penicillin–streptomycin (100 μg/mL) for 2 hours. Cells were then washed three times
638 with PBS and maintained in antibiotic-free medium until harvest. To count intracellular
639 bacteria, macrophages were lysed with 0.25% SDS for 10 minutes at room
640 temperature. Lysates were serially diluted in PBS, and 100 μL aliquots of each dilution
641 were plated on Middlebrook 7H10 agar supplemented with 10% OADC and kanamycin
642 (50 μg/mL). Plates were incubated at 37 °C for 14 days. CFUs were enumerated, and
643 final counts were calculated by applying the corresponding dilution factors. *M. bovis*
644 BCG strains used in this study are listed in Table S5.

645 **Animal experiments**

646 Specific pathogen-free (SPF) female C57BL/6 mice (6–8 weeks old, 16–18 g) were
647 obtained from Chang-sheng Bio (Liaoning, China). All animals were maintained under
648 SPF conditions in individually ventilated cages with controlled temperature and
649 humidity, on a 12-hour light/dark cycle. Mice had ad libitum access to sterilized food
650 and water.

651 **Mice infection**

652 Mice were infected as described previously (Chen *et al.,* 2022), with minor
653 modifications. Mid-log phase *M. bovis* BCG cultures were washed twice in PBS
654 containing 0.05% Tween 80 and briefly sonicated to disrupt bacterial clumps. Female
655 C57BL/6 mice were anesthetized with isoflurane and intranasally inoculated with
656 1×10^7 CFUs of *M. bovis* BCG in 40 μL of PBS. To confirm the inoculation dose, six
657 mice were euthanized at 48 hours post-infection. Lungs were harvested, homogenized
658 in 1 mL of PBS using a tissue homogenizer, and serial dilutions of the homogenates
659 were plated on Middlebrook 7H10 agar supplemented with 10% OADC. Plates were
660 incubated at 37 °C with 5% CO_2 for 14 days, after which CFUs were enumerated.

661 **Histological analysis**

662 Lung tissues from *M. bovis* BCG-infected mice were fixed in 4% phosphate-buffered
663 formalin at room temperature for 24 h, followed by paraffin embedding. Paraffin-
664 embedded tissue samples were sectioned into 2–3 μm thick slices using a microtome.
665 Sections were deparaffinized, rehydrated through a graded ethanol series, and stained

with hematoxylin and eosin (H&E). Stained tissue sections were examined using an Olympus BX53 light microscope. For digital analysis and annotation, scanned slides were visualized using CaseViewer software (version 2.0; 3DHISTECH).

Ethics approval

All animal experiments were conducted in accordance with the protocols approved by the Animal Ethics Committee of the Huazhong Agricultural University.

Statistical analyses

Data are presented as mean ± standard deviation (SD). Statistical comparisons between two groups were performed using two-tailed unpaired Student's *t*-tests, following verification of normal distribution. A *P*-value less than 0.05 was considered statistically significant. Significance levels are indicated in figures as follows: $P > 0.05$ (ns, not significant), $P < 0.05$ (*), $P < 0.01$ (**), and $P < 0.001$ (***). All statistical analyses were performed using GraphPad Prism (version 8.0). Data were obtained from at least three independent biological replicates, each including two or more technical replicates.

Acknowledgments

This work was supported by the Fundamental Research Funds for the Central Universities (#2662023DKQD001), Talent Start-up Funds of Huazhong Agricultural University (#11042310008), National Natural Science Foundation of China (#32473123), China Agriculture Research System of MOF and MARA (#CARS-37), and National Key Research and Development Program of China (#2021YFD1800403).

Author contributions

Conceptualization: L. C., A. G., and L. Z.; Methodology: L. C.; Validation: L. C., B. D., and Q. J.; Formal analysis: L. C., Y. W.; Investigation: L. C., B. D., Q. J., and Y. W.; Resources: A. G., L. Z., and Y. C.; Data curation: L. C., Q. J., and Y. W.; Writing - original draft: L. C., L. Z., and A. G.; Writing - review & editing: L. C., L. Z., and A. G.; Visualization: L. C., Q. J., Y. C., L. Z., and A. G.; Supervision: A. G., and L. Z.; Project administration: A. G., and L. Z.; Funding acquisition: A. G., L. Z., and Y. C.

694 **Disclosure and competing interest statement**

695 The authors declare no competing interests.

696 **References**

697 Agarwal S, Agarwal S, Jin H, Pancholi P, Pancholi V (2012) **Serine/threonine**
698 **phosphatase (SP-STP), secreted from Streptococcus pyogenes, is a pro-**
699 **apoptotic protein** *J Biol Chem* **287**:9147-67.

700 Aggeletopoulou I, Thomopoulos K, Mouzaki A, Triantos C (2022) **Vitamin D-VDR**
701 **novel anti-inflammatory molecules-new insights into their effects on liver**
702 **diseases** *Int J Mol Sci* **23**:8465.

703 Alsayed SSR, Gunosewoyo H (2024) **Combating Tuberculosis via restoring the**
704 **host immune capacity by targeting Mtb kinases and phosphatases** *Int J Mol Sci*
705 **25**:12481.

706 Baruch K, Gur-Arie L, Nadler C, Koby S, Yerushalmi G, Ben-Neriah Y, Yogev O,
707 Shaulian E, Guttman C, Zarivach R, Rosenshine I (2011) **Metalloprotease type III**
708 **effectors that specifically cleave JNK and NF-κB** *EMBO J* **30**:221-31.

709 Bhadouria J, Giri J (2022) **Purple acid phosphatases: roles in phosphate utilization**
710 **and new emerging functions** *Plant Cell Rep* **41**:33-51.

711 Bhadouria J, Singh AP, Mehra P, Verma L, Srivastawa R, Parida SK, Giri J (2017)
712 **Identification of purple acid phosphatases in chickpea and potential roles of**
713 **CaPAP7 in seed phytate accumulation** *Sci Rep* **7**:11012.

714 Bierne H, Cossart P (2021) **When bacteria target the nucleus: the emerging family**
715 **of nucleomodulins** *Cell Microbiol* **14**:622-33.

716 Bonne Køhler J, Jers C, Senissar M, Shi L, Derouiche A, Mijakovic I (2020)
717 **Importance of protein Ser/Thr/Tyr phosphorylation for bacterial pathogenesis**
718 *FEBS Lett* **594**:2339-2369.

719 Buchanan G, Sargent F, Berks BC, Palmer T (2001) **A genetic screen for**
720 **suppressors of *Escherichia coli* Tat signal peptide mutations establishes a**
721 **critical role for the second arginine within the twin-arginine motif** *Arch Microbiol*
722 **177**:107-12.

723 Cautain B, Hill R, de Pedro N, Link W (2015) **Components and regulation of nuclear**
724 **transport processes** *FEBS J* **282**:445-62.

725 Chai Q, Wang L, Liu CH, Ge B (2020) **New insights into the evasion of host innate**
726 **immunity by *Mycobacterium tuberculosis*** *Cell Mol Immunol* **17**:901-913.

727 Chandra P, Grigsby SJ, Philips JA (2022) **Immune evasion and provocation by**
728 ***Mycobacterium tuberculosis*** *Nat Rev Microbiol* **20**:750-766.

729 Chen L, Duan B, Chen P, Jiang Q, Wang Y, Lu L, Chen Y, Hu C, Zhang L, Guo A (2025)
730 **A conserved mycobacterial nucleomodulin hijacks the host COMPASS complex**
731 **to reprogram pro-inflammatory transcription and promote intracellular survival**
732 *bioRxiv* https://doi.org/10.1101/2025.05.21.655295

733 Chen L, Li X, Xu P, He ZG (2022) **A novel zinc exporter CtpG enhances resistance**
734 **to zinc toxicity and survival in *Mycobacterium bovis*** *Microbiol Spectr*
735 10:e0145621.

736 Chen Y, Du J, Zhang Z, Liu T, Shi Y, Ge X, Li YC (2014) **MicroRNA-346 mediates**
737 **tumor necrosis factor α-induced downregulation of gut epithelial vitamin D**
738 **receptor in inflammatory bowel diseases** *Inflamm Bowel Dis* **20**:1910-8.

739 Comba S, Menendez-Bravo S, Arabolaza A, Gramajo H (2013) **Identification and**
740 **physiological characterization of phosphatidic acid phosphatase enzymes**
741 **involved in triacylglycerol biosynthesis in *Streptomyces coelicolor*** *Microb Cell*
742 *Fact* **12**:9.

743 Davicino RC, Méndez-Huergo SP, Eliçabe RJ, Stupirski JC, Autenrieth I, Di Genaro
744 MS, Rabinovich GA (2017) **Galectin-1-driven tolerogenic programs**

745 **aggravate *Yersinia enterocolitica* infection by repressing antibacterial Immunity**
746 *J Immunol* **199**:1382-1392.

747 Dean P, Scott JA, Knox AA, Quitard S, Watkins NJ, Kenny B (2010) **The**
748 **enteropathogenic *E. coli* effector EspF targets and disrupts the nucleolus by a**
749 **process regulated by mitochondrial dysfunction** *PLoS Pathog* **6**:e1000961.

750 Evans SM, Rodino KG, Adcox HE, Carlyon JA (2018) ***Orientia tsutsugamushi* uses**
751 **two Ank effectors to modulate NF-κB p65 nuclear transport and inhibit NF-κB**
752 **transcriptional activation** *PLoS Pathog* **14**:e1007023.

753 Fang S, Wan X, Zou X, Sun S, Hao X, Liang C, Zhang Z, Zhang F, Sun B, Li H, Yu B
754 (2021) **Arsenic trioxide induces macrophage autophagy and atheroprotection by**
755 **regulating ROS-dependent TFEB nuclear translocation and AKT/mTOR pathway**
756 *Cell Death Dis* **12**:88.

757 Feder D, McGeary RP, Mitić N, Lonhienne T, Furtado A, Schulz BL, Henry RJ, Schmidt
758 S, Guddat LW, Schenk G (2020) **Structural elements that modulate the substrate**
759 **specificity of plant purple acid phosphatases: Avenues for improved**
760 **phosphorus acquisition in crops** *Plant Sci* **294**:110445.

761 Fontes MR, Teh T, Kobe B (2000) **Structural basis of recognition of monopartite**
762 **and bipartite nuclear localization sequences by mammalian importin-alpha** *J Mol*
763 *Biol* **297**:1183-94.

764 Forrellad MA, Blanco FC, Marrero Diaz de Villegas R, Vázquez CL, Yaneff A, García
765 EA, Gutierrez MG, Durán R, Villarino A, Bigi F (2020) **Rv2577 of *Mycobacterium***
766 ***tuberculosis* Is a virulence factor with dual phosphatase and phosphodiesterase**
767 **functions** *Front Microbiol* **11**:570794.

768 Ge P, Lei Z, Yu Y, Lu Z, Qiang L, Chai Q, Zhang Y, Zhao D, Li B, Pang Y, Liu CH, Wang
769 J (2022) ***M. tuberculosis* PknG manipulates host autophagy flux to promote**
770 **pathogen intracellular survival** *Autophagy* **18**:576-594.

771 Gimenez MR, Chandra G, Van Overvelt P, Voulhoux R, Bleves S, Ize B (2018)
772 **Genome wide identification and experimental validation of *Pseudomonas***
773 ***aeruginosa* Tat substrates** *Sci Rep* **8**:11950.

774 Gounis M, Hamidi H, Ivaska J (2025) **mTORC1 shutdown unleashes TFEB to drive**
775 **triple-negative breast cancer invasion** *Dev Cell* **60**:979-981.

776 Hanford HE, Von Dwingelo J, Abu Kwaik Y (2021) **Bacterial nucleomodulins: a**
777 **coevolutionary adaptation to the eukaryotic command center** *PLoS Pathog*
778 **17**:e1009184.

779 Hodgson A, Wier EM, Fu K, Sun X, Yu H, Zheng W, Sham HP, Johnson K, Bailey S,
780 Vallance BA, Wan F (2015) **Metalloprotease NleC suppresses host NF-**
781 **κB/inflammatory responses by cleaving p65 and interfering with the p65/RPS3**
782 **interaction** *PLoS Pathog* **11**:e1004705.

783 Jeong SJ, Stitham J, Evans TD, Zhang X, Rodriguez-Velez A, Yeh YS, Tao J,
784 Takabatake K, Epelman S, Lodhi IJ, Schilling JD, DeBosch BJ, Diwan A, Razani B
785 (2021) **Trehalose causes low-grade lysosomal stress to activate TFEB and the**
786 **autophagy-lysosome biogenesis response**. Autophagy **17**:3740-3752.

787 Jermy A (2010) **Chlamydia gets a NUE look** *Nat Rev Microbiol*. **8**:614.

788 Jose L, Ramachandran R, Bhagavat R, Gomez RL, Chandran A, Raghunandanan S,
789 Omkumar RV, Chandra N, Mundayoor S, Kumar RA (2016) **Hypothetical protein**
790 **Rv3423.1 of *Mycobacterium tuberculosis* is a histone acetyltransferase** *FEBS J*
791 **283**:265-81.

792 Kosugi S, Hasebe M, Matsumura N, Takashima H, Miyamoto-Sato E, Tomita M,
793 Yanagawa H (2009) **Six classes of nuclear localization signal specific to different**
794 **binding grooves of importin alpha** *J Biol Chem* **284**:478-485.

795 Kurucz V, Krüger T, Antal K, Dietl AM, Haas H, Pócsi I, Kniemeyer O, Emri T (2018)
796 **Additional oxidative stress reroutes the global response of *Aspergillus***
797 ***fumigatus* to iron depletion** *BMC Genomics* **19**:357.

798 Lange A, Mills RE, Devine SE, Corbett AH (2008) **A PY-NLS nuclear targeting signal**
799 **is required for nuclear localization and function of the *Saccharomyces***
800 ***cerevisiae* mRNA-binding protein Hrp1** *J Biol Chem* **283**:12926-34.

801 Lebreton A, Job V, Ragon M, Le Monnier A, Dessen A, Cossart P, Bierne H (2014)
802 **Structural basis for the inhibition of the chromatin repressor BAHD1 by the**
803 **bacterial nucleomodulin LntA** *mBio* **5**: e00775-13.

804 Lebreton A, Lakisic G, Job V, Fritsch L, Tham TN, Camejo A, Matteï PJ, Regnault B,
805 Nahori MA, Cabanes D, Gautreau A, Ait-Si-Ali S, Dessen A, Cossart P, Bierne H (2011)
806 **A bacterial protein targets the BAHD1 chromatin complex to stimulate type III**
807 **interferon response** *Science* **331**:1319-21.

808 Li T, Lu Q, Wang G, Xu H, Huang H, Cai T, Kan B, Ge J, Shao F (2013) **SET-domain**
809 **bacterial effectors target heterochromatin protein 1 to activate host rDNA**
810 **transcription** *EMBO Rep* **14**:733-40.

811 Li X, Chen L, Liao J, Hui J, Li W, He ZG (2020) **A novel stress-inducible CmtR-ESX3-**
812 **Zn^{2+} regulatory pathway essential for survival of *Mycobacterium bovis* under**
813 **oxidative stress** *J Biol Chem* **295**:17083-17099.

814 Li X, Zhang M, Zhou G, Xie Z, Wang Y, Han J, Li L, Wu Q, Zhang S (2023) **Role of**
815 **Rho GTPases in inflammatory bowel disease** *Cell Death Discov* **9**:24.

816 Liu PT, Stenger S, Li H, Wenzel L, Tan BH, Krutzik SR, Ochoa MT, Schauber J, Wu K,
817 Meinken C, Kamen DL, Wagner M, Bals R, Steinmeyer A, Zügel U, Gallo RL,
818 Eisenberg D, Hewison M, Hollis BW, Adams JS, Bloom BR, Modlin RL (2006) **Toll-like**
819 **receptor triggering of a vitamin D-mediated human antimicrobial response**
820 *Science* **311**:1770-3.

821 Liu SF, Yi ZC, Huang ZQ, Yuan ZD, Yang YC, Zhao Y, He QY, Yang WD, Li HY, Lin
822 CSK, Wang X (2025) **Enhanced biodegradation of glyphosate by *Chlorella***
823 ***sorokiniana* engineered with exogenous purple acid phosphatase** *Water Res*
824 **268**:122737.

825 Lu J, Wu T, Zhang B, Liu S, Song W, Qiao J, Ruan H (2021) **Types of nuclear**
826 **localization signals and mechanisms of protein import into the nucleus** *Cell*
827 *Commun Signal* **19**:60.

828 Ma S, Ming Y, Wu J, Cui G (2024) **Cellular metabolism regulates the differentiation**
829 **and function of T-cell subsets** *Cell Mol Immunol* **21**:419-435.

830 Manfiolli AO, de Castro PA, Dos Reis TF, Dolan S, Doyle S, Jones G, Riaño Pachón
831 DM, Ulaş M, Noble LM, Mattern DJ, Brakhage AA, Valiante V, Silva-Rocha R, Bayram
832 O, Goldman GH (2017) ***Aspergillus fumigatus*** **protein phosphatase PpzA is**
833 **involved in iron assimilation, secondary metabolite production, and virulence**
834 *Cell Microbiol* **19**.

835 Mitra S, Dunphy PS, Das S, Zhu B, Luo T, McBride JW (2018) ***Ehrlichia chaffeensis***
836 **TRP120 effector targets and recruits host polycomb group proteins for**
837 **degradation to promote intracellular infection** *Infect Immun* **86**:e00845-17.

838 Nasiri MJ, Venketaraman V (2025) **Advances in host-pathogen interactions in**
839 **Tuberculosis: emerging strategies for therapeutic intervention** *Int J Mol Sci*
840 **26**:1621.

841 Nisa A, Kipper FC, Panigrahy D, Tiwari S, Kupz A, Subbian S (2022) **Different**
842 **modalities of host cell death and their impact on *Mycobacterium tuberculosis***
843 **infection** *Am J Physiol Cell Physiol* **323**:C1444-C1474.

844 Pennini ME, Perrinet S, Dautry-Varsat A, Subtil A (2010) **Histone methylation by NUE,**
845 **a novel nuclear effector of the intracellular pathogen *Chlamydia trachomatis***
846 *PLoS Pathog* **6**:e1000995.

847 Rodriguez F, Lillington J, Johnson S, Timmel CR, Lea SM, Berks BC (2014) **Crystal**
848 **structure of the *Bacillus subtilis* phosphodiesterase PhoD reveals an iron and**
849 **calcium-containing active site** *J Biol Chem* **289**:30889-99.

850 Rolando M, Sanulli S, Rusniok C, Gomez-Valero L, Bertholet C, Sahr T, Margueron R,
851 Buchrieser C (2013) ***Legionella pneumophila*** **effector RomA uniquely modifies**

852 **host chromatin to repress gene expression and promote intracellular bacterial**
853 **replication** *Cell Host Microbe* **13**:395-405.

854 Sajid A, Arora G, Singhal A, Kalia VC, Singh Y (2015) **Protein phosphatases of**
855 **pathogenic bacteria: role in physiology and virulence** *Annu Rev Microbiol* **69**:527-
856 47.

857 Schenk G, Guddat LW, Ge Y, Carrington LE, Hume DA, Hamilton S, de Jersey J (2000)
858 **Identification of mammalian-like purple acid phosphatases in a wide range of**
859 **plants** *Gene* **250**:117-25.

860 Shaban L, Nguyen GT, Mecsas-Faxon BD, Swanson KD, Tan S, Mecsas J (2020)
861 ***Yersinia pseudotuberculosis* YopH targets SKAP2-dependent and independent**
862 **signaling pathways to block neutrophil antimicrobial mechanisms during**
863 **infection** *PLoS Pathog* **16**:e1008576.

864 Singh AP, Sharma S, Pagarware K, Siraji RA, Ansari I, Mandal A, Walling P, Aijaz S
865 (2018) **Enteropathogenic *E. coli* effectors EspF and Map independently disrupt**
866 **tight junctions through distinct mechanisms involving transcriptional and post-**
867 **transcriptional regulation** *Sci Rep* **8**:3719.

868 Singh PR, Dadireddy V, Udupa S, Kalladi SM, Shee S, Khosla S, Rajmani RS, Singh
869 A, Ramakumar S, Nagaraja V (2023) **The *Mycobacterium tuberculosis***
870 **methyltransferase Rv2067c manipulates host epigenetic programming to**
871 **promote its own survival** *Nat Commun* **14**:8497.

872 Singh PR, Nagaraja V (2025) **Epigenetic maneuvering: an emerging strategy for**
873 **mycobacterial intracellular survival** *Trends Microbiol* **33**:354-369.

874 Stanley NR, Palmer T, Berks BC (2000) **The twin arginine consensus motif of Tat**
875 **signal peptides is involved in Sec-independent protein targeting in *Escherichia***
876 ***coli*** *J Biol Chem* **275**:11591-6.

877 Steiert B, Weber MM (2025) **Nuclear warfare: pathogen manipulation of the**
878 **nuclear pore complex and nuclear functions** *mBio* **16**:e0194024.

879 Tang D, Chen M, Huang X, Zhang G, Zeng L, Zhang G, Wu S, Wang Y (2023) **SRplot:**
880 **A free online platform for data visualization and graphing** *PLoS One* **18**:e0294236.

881 Ulfig A, Fröbel J, Lausberg F, Blümmel AS, Heide AK, Müller M, Freudl R (2017) **The**
882 **h-region of twin-arginine signal peptides supports productive binding of**
883 **bacterial Tat precursor proteins to the TatBC receptor complex** *J Biol Chem*
884 **292**:10865-10882.

885 Usategui-Martín R, De Luis-Román DA, Fernández-Gómez JM, Ruiz-Mambrilla M,
886 Pérez-Castrillón JL (2022) **Vitamin D receptor (VDR) gene polymorphisms modify**
887 **the response to vitamin d supplementation: a systematic review and meta-**
888 **analysis** *Nutrients* **14**:360.

889 Wang B, Martini-Stoica H, Qi C, Lu TC, Wang S, Xiong W, Qi Y, Xu Y, Sardiello M, Li
890 H, Zheng H (2024) **TFEB-vacuolar ATPase signaling regulates lysosomal function**
891 **and microglial activation in tauopathy** *Nat Neurosci* **27**:48-62.

892 Wang J, Ge P, Qiang L, Tian F, Zhao D, Chai Q, Zhu M, Zhou R, Meng G, Iwakura Y,
893 Gao GF, Liu CH (2017) **The mycobacterial phosphatase PtpA regulates the**
894 **expression of host genes and promotes cell proliferation** *Nat Commun* **8**:244.

895 Wong D, Bach H, Sun J, Hmama Z, Av-Gay Y (2011) ***Mycobacterium tuberculosis***
896 **protein tyrosine phosphatase (PtpA) excludes host vacuolar-H^+-ATPase to**
897 **inhibit phagosome acidification** *Proc Natl Acad Sci U S A* **108**:19371-6.

898 Yeung SL, Cheng C, Lui TK, Tsang JS, Chan WT, Lim BL (2009) **Purple acid**
899 **phosphatase-like sequences in prokaryotic genomes and the characterization of**
900 **an atypical purple alkaline phosphatase from *Burkholderia cenocepacia* J2315**
901 *Gene* **440**:1-8.

902 Zhang QA, Ma S, Li P, Xie J (2023) **The dynamics of *Mycobacterium tuberculosis***
903 **phagosome and the fate of infection** *Cell Signal* **108**:110715.

904 Zhang W, Dong C, Xiong S (2024) **Mycobacterial SapM hampers host autophagy**
905 **initiation for intracellular bacillary survival via dephosphorylating Raptor**
906 *iScience* **27**:109671.

907

908

909

910

911

912

913

914

915

916

917

918

919

920

921

922

923

924

925

926

927 **Legends**

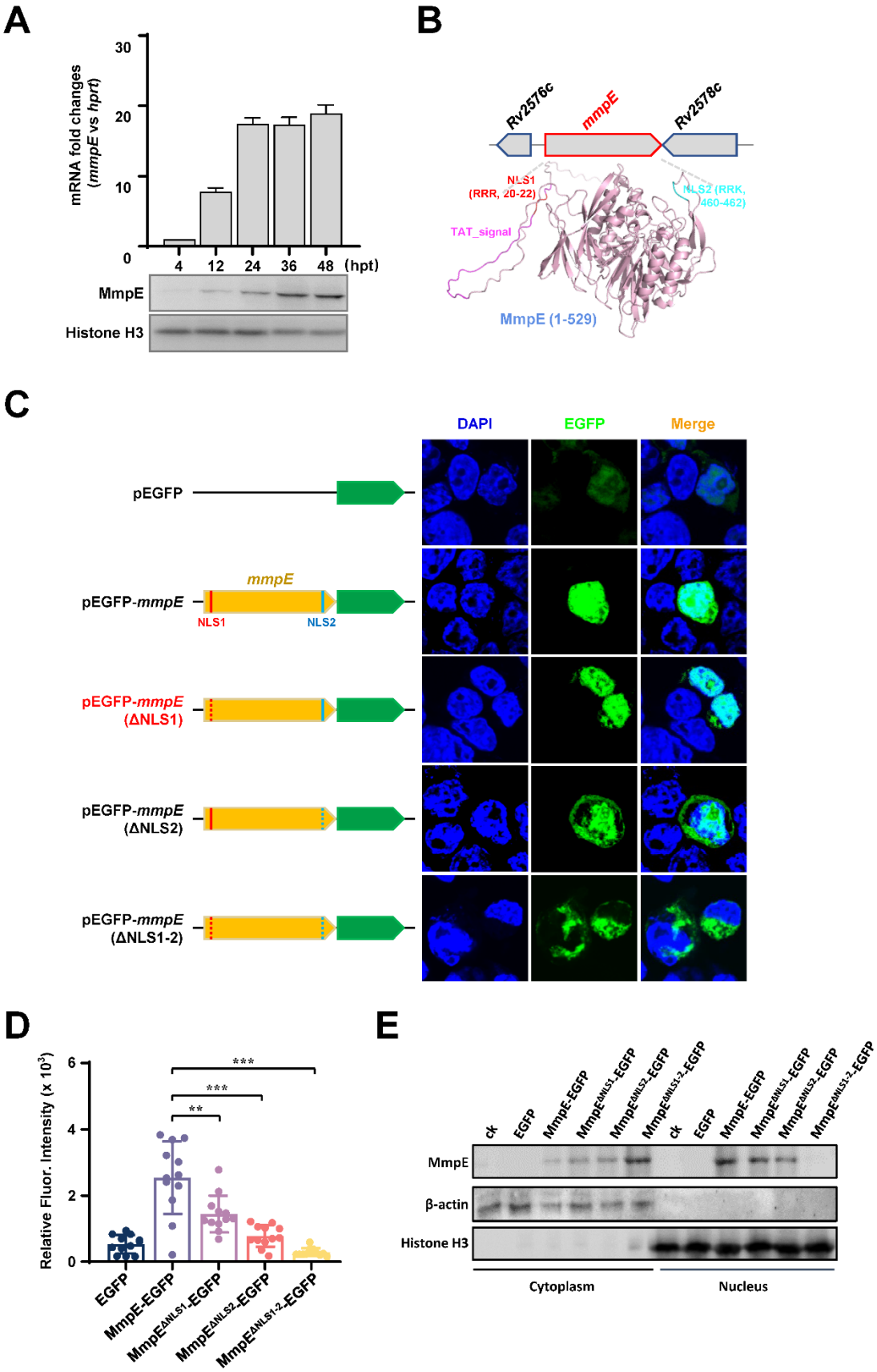

928

929 **Figure 1. NLSs are required for the nuclear translocation of MmpE.**

930 **(A)** Expression and nuclear localization of *MmpE*. (upper) qRT-PCR analysis of *mmpE*
931 mRNA in HEK293T cells over 48 h post-transfection. (bottom) Western blot analysis of
932 nuclear fractions showing time-dependent nuclear accumulation of MmpE-EGFP.
933 Histone H3 and β-actin served as nuclear and cytoplasmic markers, respectively.

934 **(B)** Domain architecture of MmpE. The schematic representation of MmpE shows its
935 annotated functional domains, including a Tat signal peptide (1-54 amino acids, with a
936 twin-arginine translocation motif) and two nuclear localization signals (NLS1: 20-22
937 amino acids; NLS2: 460-462 amino acids). The structure of the MmpE protein was
938 predicted using AlphaFold 2.2.0, where the position of NLS1 is highlighted in red and
939 NLS2 is highlighted in green.

940 **(C)** Subcellular localization of EGFP-tagged wild-type and NLS-deleted MmpE. (left)
941 Schematic representation of EGFP-tagged constructs, including wild-type MmpE and
942 its mutants ($MmpE^{\Delta NLS1}$, $MmpE^{\Delta NLS2}$, and $MmpE^{\Delta NLS1\text{-}2}$). (right) Confocal microscopy
943 images of HEK293T cells transfected with the indicated constructs for 36 hpt. EGFP
944 fluorescence (green) and nuclear staining with DAPI (blue) were visualized using an
945 FLUOVIEW software (v5.0). Scale bar, 10 μm. Images were acquired with a ×100 oil
946 immersion objective (NA = 1.4).

947 (**D**) Nuclear EGFP intensity of wild-type and mutant constructs in **(C)**. Data are shown
948 as mean ± SD (n = 12 cells).

949 (**E**) Western blot analysis of nuclear and cytoplasmic fractions from HEK293T cells
950 transfected with wild-type and mutant MmpE-EGFP confirmed their nuclear
951 localization. MmpE-EGFP was detected using an anti-GFP antibody, and histone H3
952 and β-actin served as nuclear and cytoplasmic markers, respectively.

953 All experiments were performed in three biologically independent replicates. Statistical
954 significance was assessed by two-tailed unpaired Student's *t*-tests, with $^{*}P < 0.05$
955 considered statistically significant.

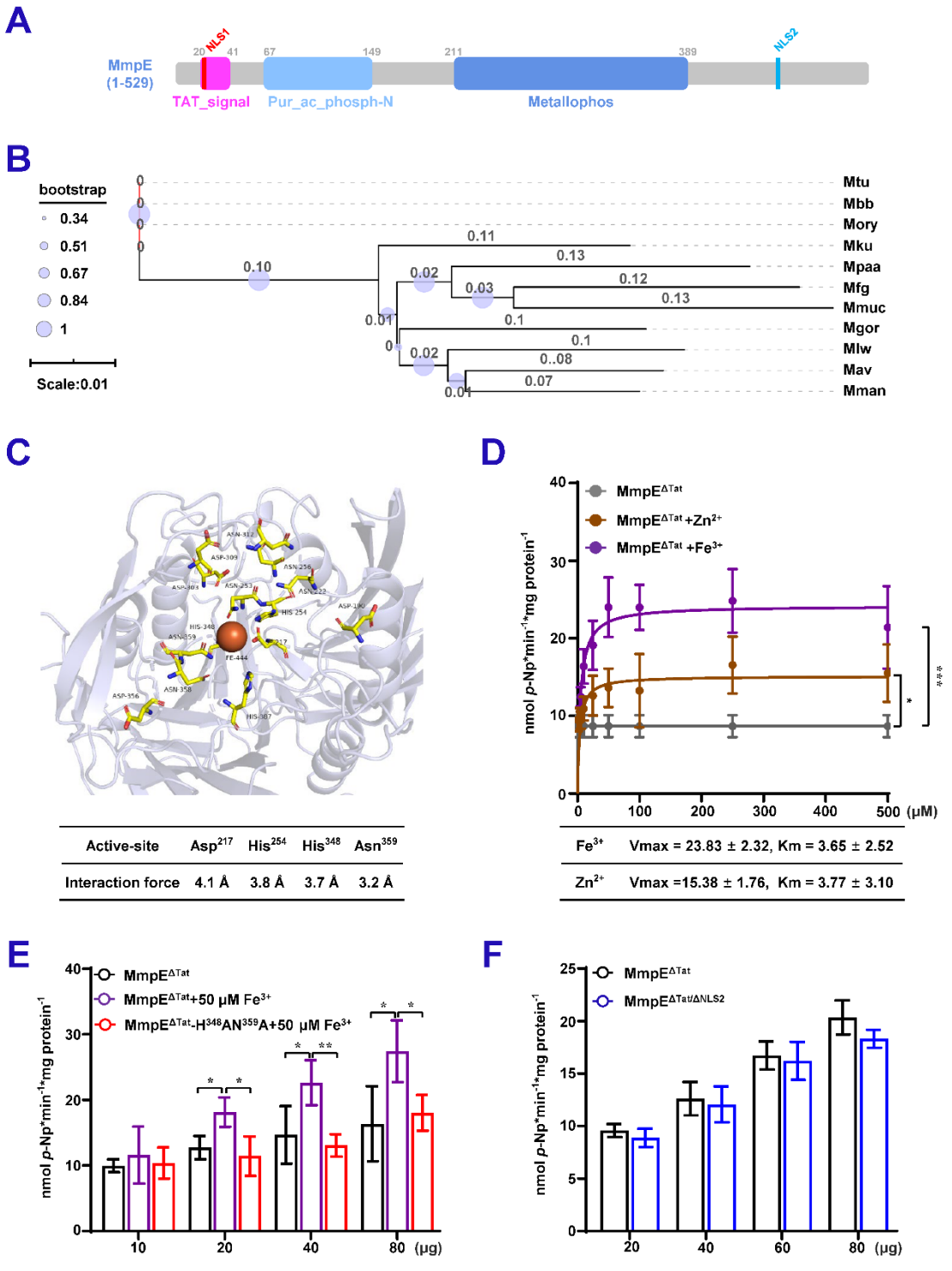

Figure 2. Deletion of NLSs does not alter the phosphatase activity of MmpE. (**A**) Domain architecture of MmpE. Schematic representation of MmpE with the annotated functional domains, including a Tat signal peptide (1–41 aa, twin-arginine translocation motif), a purple acid phosphatase domain (68–149 aa), a calcineurin-like phosphoesterase domain (211–389 aa) and two nuclear localization signals (NLS1:

20-22 aa; NLS2: 460–462 aa).

(**B**) Phylogenetic and structural conservation of MmpE. Neighbor-joining phylogenetic tree of MmpE homologs across Mycobacterium species (1,000 bootstrap replicates; values ≥50% shown). Species abbreviations: *M. tuberculosis* (Mtu), *M. bovis* BCG (Mbb), *M. orygis* (Mory), *M. kubicae* (Mku), *M. paraterrae* (Mpaa), *M. farcinogenes* (Mfg), *M. mucogenicum* (Mmuc), *M. vicinigordonae* (Mgor), *M. lentiflavum* (Mlw), *M. avium* (Mav), *M. manitobense* (Mman).

(C) Prediction of metal ion-binding residues in MmpE. Structural modeling and visualization of MmpE were performed using PyMOL. Conserved residues located in the putative metal binding pocket are shown as sticks and colored according to atom type. The predicted metal coordination site is highlighted, and key residues potentially involved in metal ion binding are labeled. Surface representation is included to illustrate the spatial accessibility of the binding pocket.

(D-F) Phosphatase activity assays of $MmpE^{\Delta Tat}$ under various conditions. Phosphatase activity of $MmpE^{\Delta Tat}$ (lacking the N-terminal Tat signal peptide) was measured using *p*-nitrophenyl phosphate (*p*-NPP) as the substrate in the presence of increasing concentrations (0–500 μM) of Fe^{3+} and Zn^{2+} (**D**). Phosphatase activity of increasing concentrations of $MmpE^{\Delta Tat}$ and the mutant $MmpE^{\Delta Tat}$-$H^{348}AN^{359}A$ was measured in the absence or presence of 50 μM Fe^{3+} (**E**). Phosphatase activity of increasing concentrations of $MmpE^{\Delta Tat}$ and the double-NLS deletion mutant $MmpE^{\Delta Tat/\Delta NLS1\text{-}2}$ was measured under standard conditions (**F**).

Data represent mean ± SD of three biologically independent experiments, analyzed using two-tailed unpaired Student's *t*-tests (**P* < 0.05, ***P* < 0.01, ****P* < 0.001).

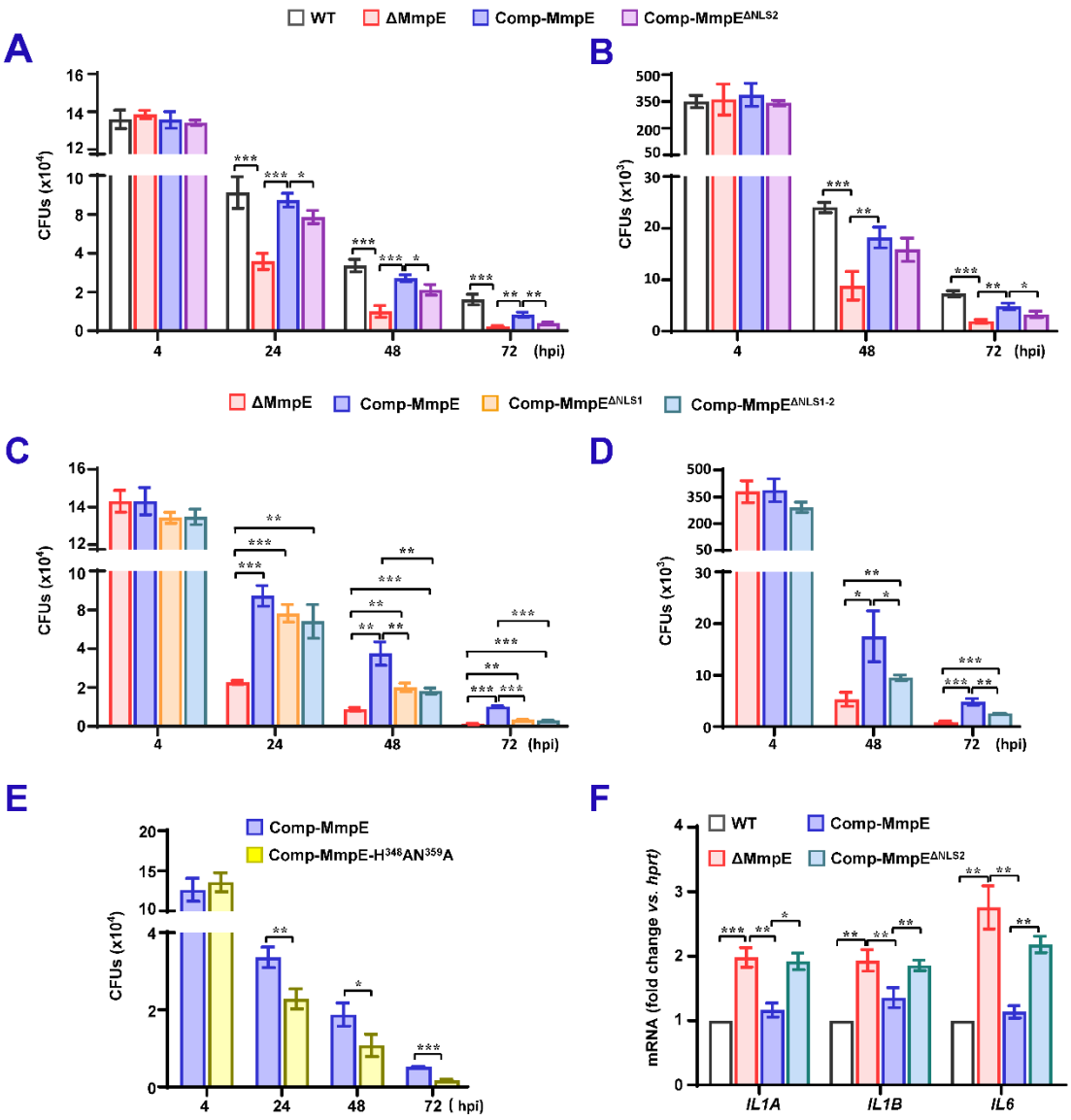

Figure 3. The nuclear translocation and phosphatase activity of MmpE are essential for *M. bovis* BCG survival in macrophage cells.

(A–B) Intracellular survival of *M. bovis* BCG strains in human THP-1 macrophages (**A**) and murine RAW264.7 macrophages (**B**). Strains include wild-type BCG (WT), MmpE deletion mutant (ΔMmpE), wild-type MmpE complemented strain (Comp-MmpE), and NLS2-deleted complement strain (Comp-MmpE$^{\Delta NLS2}$).

(C–D) Intracellular survival of *M. bovis* BCG strains in THP-1 (**C**) and RAW264.7 (**D**) macrophages. Strains include ΔMmpE, Comp-MmpE, and NLS-deficient complement strains (Comp-MmpE$^{\Delta NLS1}$ and Comp-MmpE$^{\Delta NLS1\text{-}2}$).

(E) Intracellular survival of metal ion binding site mutants in THP-1 cells. Strains include Comp-MmpE and a phosphatase-deficient mutant (Comp-MmpE-H^{348}AN^{359}H).

997 **(F)** Inflammatory cytokine expression in infected THP-1 cells. mRNA levels of *IL-1α*,
998 *IL-1β*, and *IL-6* were quantified by qRT-PCR 20 hpi with the indicated BCG strains.
999 Data represent mean ± SD from three independent biological replicates. Statistical
1000 analysis was performed using two-tailed unpaired Student's *t*-tests (*$P < 0.05$, **$P <$
1001 0.01, ***$P < 0.001$).

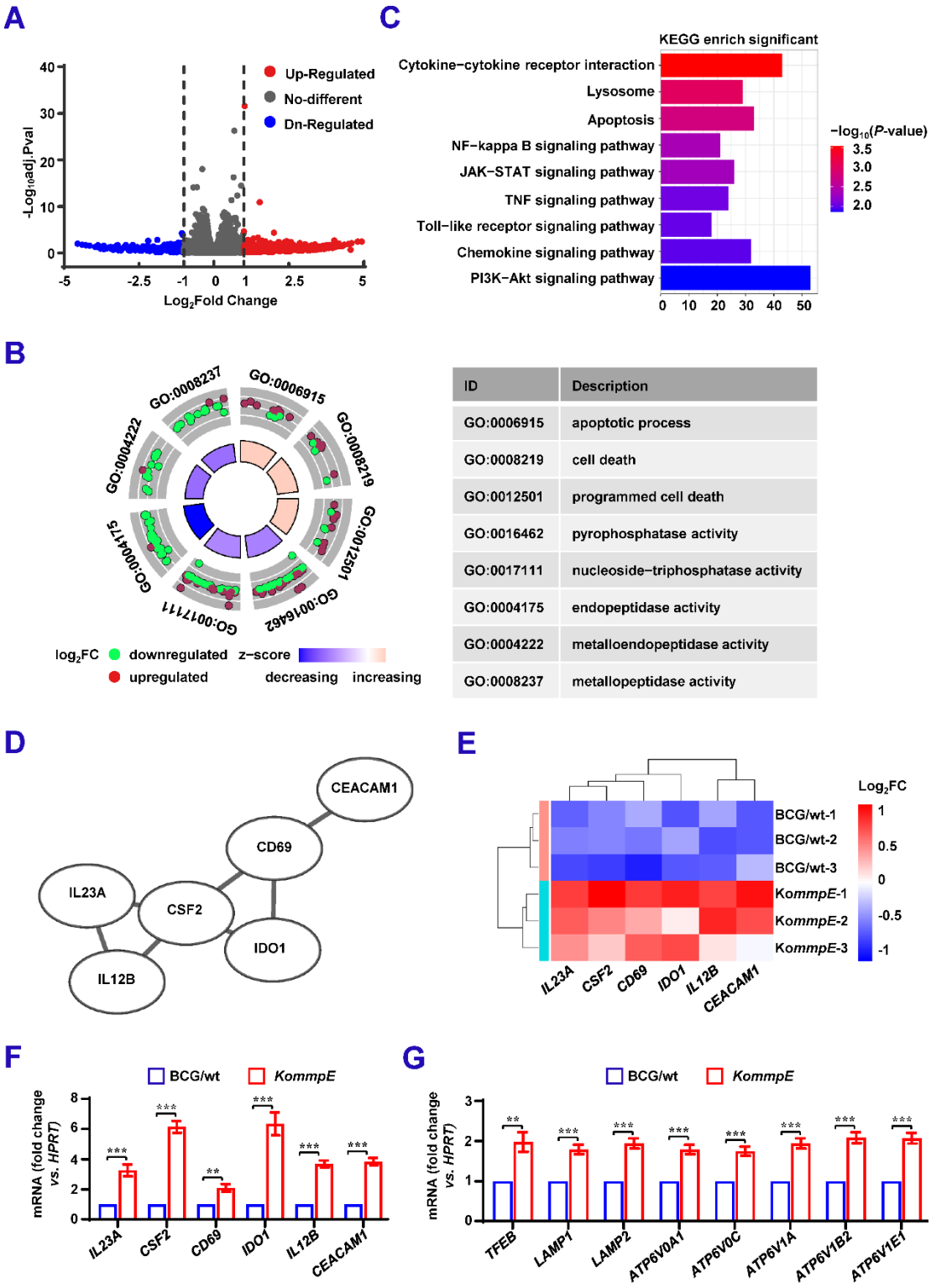

Figure 4. MmpE modulates host transcription network involved in inflammation response and lysosomal maturation.

(**A**) Volcano plot of differentially expressed genes (DEGs). DEGs in MmpE deleted strain (Ko*mmpE*) compared to wild-type BCG (BCG/wt) were visualized in a volcano

1007 plot. DEGs were defined as genes with $|\log_2(\text{fold change})| \geq 1$ and $P < 0.05$. The *x*-axis
1008 represents $\log_2$(fold change), and the *y*-axis shows $-\log_{10}$(P-value). Genes with
1009 significant upregulation and downregulation are highlighted.
1010 **(B)** GO enrichment analysis of DEGs in Ko*mmpE*-infected THP-1 cells versus BCG/wt.
1011 The circular plot shows enriched biological process and molecular function terms.
1012 Outer rings represent GO terms, with red and green dots indicating upregulated and
1013 downregulated DEGs, respectively. The inner ring color reflects z-scores (blue: low;
1014 pink: high). The table lists selected GO terms with their IDs and descriptions.
1015 **(C)** KEGG enrichment analysis of DEGs in KommpE-infected THP-1 cells versus
1016 BCG/wt. The bar plot displays selected significantly enriched pathways. Bar length
1017 represents the number of DEGs associated with each pathway, and color indicates
1018 statistical significance based on $-\log_{10}$(*P*-value).
1019 **(D)** Interaction network of DEGs related to immune regulation. Network construction
1020 was performed using STRING v12.0 and visualized with Cytoscape.
1021 (**E**) Heatmap of immune-related DEGs in Ko*mmpE*-infected and BCG/wt-infected THP-
1022 1 cells. Log_2fold change values are shown across three biological replicates. Red and
1023 blue indicate upregulation and downregulation, respectively.
1024 (**F-G**) Quantitative RT-PCR analysis of gene expression in infected THP-1 cells. THP-
1025 1 cells were infected with BCG/wt or Ko*mmpE* strains for 20 hpi. mRNA levels of
1026 cytokine genes (**F**); mRNA levels of genes involved in lysosomal acidification and
1027 biogenesis (**G**).
1028 Data are presented as mean ±SD of three biologically independent experiments,
1029 analyzed using two-tailed unpaired Student's *t*-tests (**P* < 0.05, ***P* < 0.01, and ****P* <
1030 0.001).

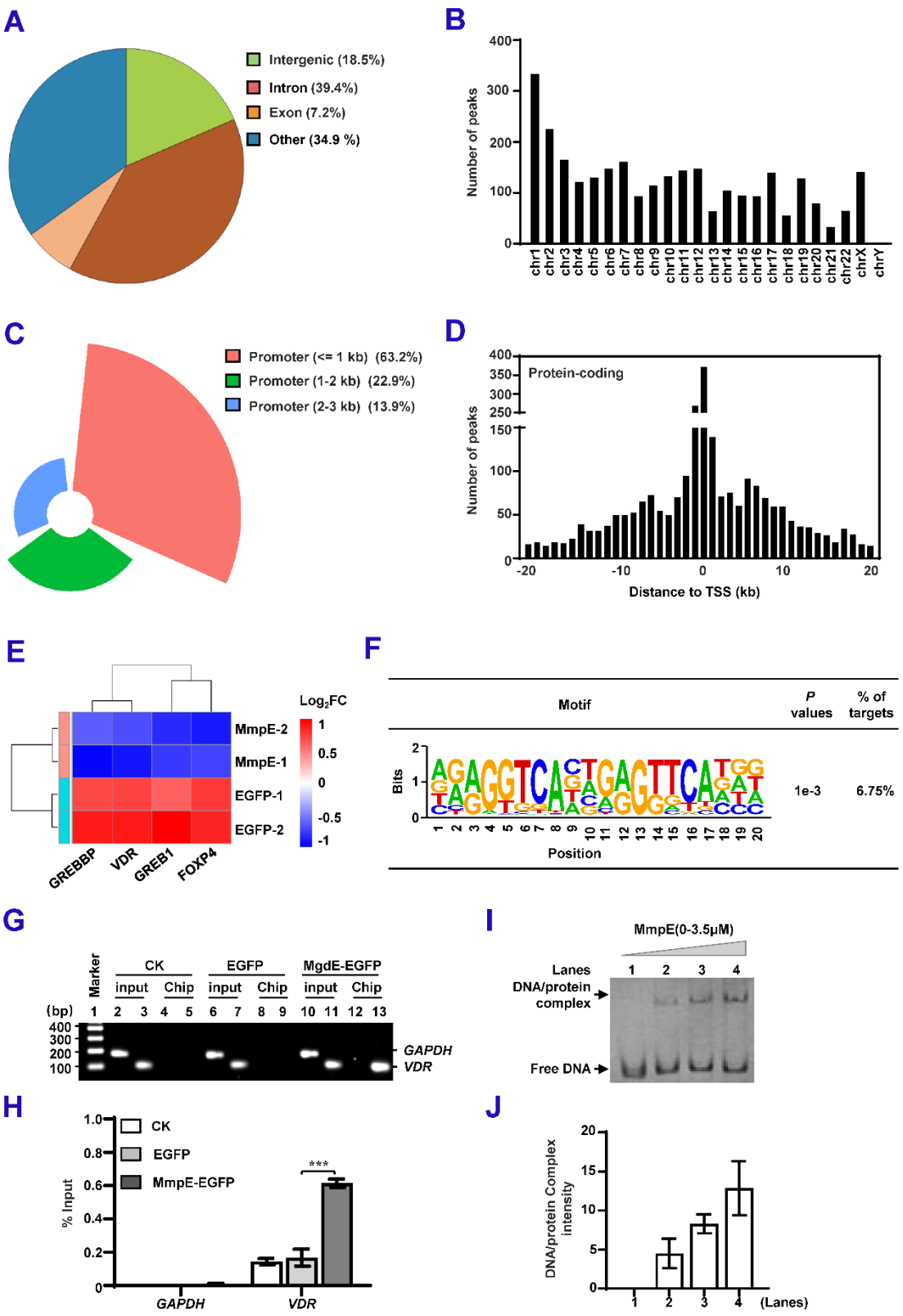

Figure 5. MmpE suppresses the expression of *VDR* and inhibits activation of the PI3K–Akt–mTOR signaling pathway.

(**A**) Genomic distribution of potential MmpE-binding regions in HEK293T cells.

1035 (**B**) Distribution of the chromosomal location of MmpE-specific ChIP-seq signals (fold-
1036 enrichment > 9).
1037 (**C**) Biotype distribution of potential MmpE-binding regions in HEK293T cells.
1038 (**D**) The number and position of the potential MmpE-binding sites along 20 kb from the
1039 nearest TSS of the protein-coding genes.
1040 (**E**) Heatmap of transcription factors identified by MmpE ChIP-seq. Colors represent
1041 expression changes, with red indicating upregulation and blue indicating
1042 downregulation.
1043 (**F**) MmpE-binding motifs identified by *de novo* motif analysis of ChIP-seq peak
1044 sequences using HOMER. Motif enrichment *P*-values were calculated using TOMTOM.
1045 "% of targets" indicates the proportion of MmpE-bound regions containing each motif.
1046 Letter height reflects the frequency of each nucleotide at the corresponding position in
1047 the consensus motif.
1048 **(G-H)** ChIP-PCR and qPCR analyses of MmpE binding to the VDR promoter region.
1049 Chromatin was immunoprecipitated from HEK293T cells transfected with control
1050 vector (CK), EGFP, or MmpE–EGFP constructs. PCR was performed using primers
1051 targeting the *GAPDH* region (negative control) and the *VDR* promoter region, and
1052 products were analyzed by agarose gel electrophoresis (**G**). ChIP enrichment for *VDR*
1053 and *GAPDH* was quantified in HEK293T cells using qPCR, with enrichment calculated
1054 by the $2^{-\Delta Ct}$ method(**H**).
1055 **(I-J)** EMSA analysis showing the binding of MmpE to the human *VDR* promoter. The
1056 formation of DNA–protein complexes was observed with increasing concentrations of
1057 MmpE protein. Arrows indicate the positions of free DNA and DNA–protein complexes
1058 on the native polyacrylamide gel (**I**). Quantitative analysis of DNA–protein complexes
1059 in each lane (**I**) was performed by densitometry (**J**).
1060 Data are presented as mean ±SD of three biologically independent experiments.
1061 Statistical significance was determined by a two-tailed unpaired Student's *t*-test (***$P <$
1062 0.001).

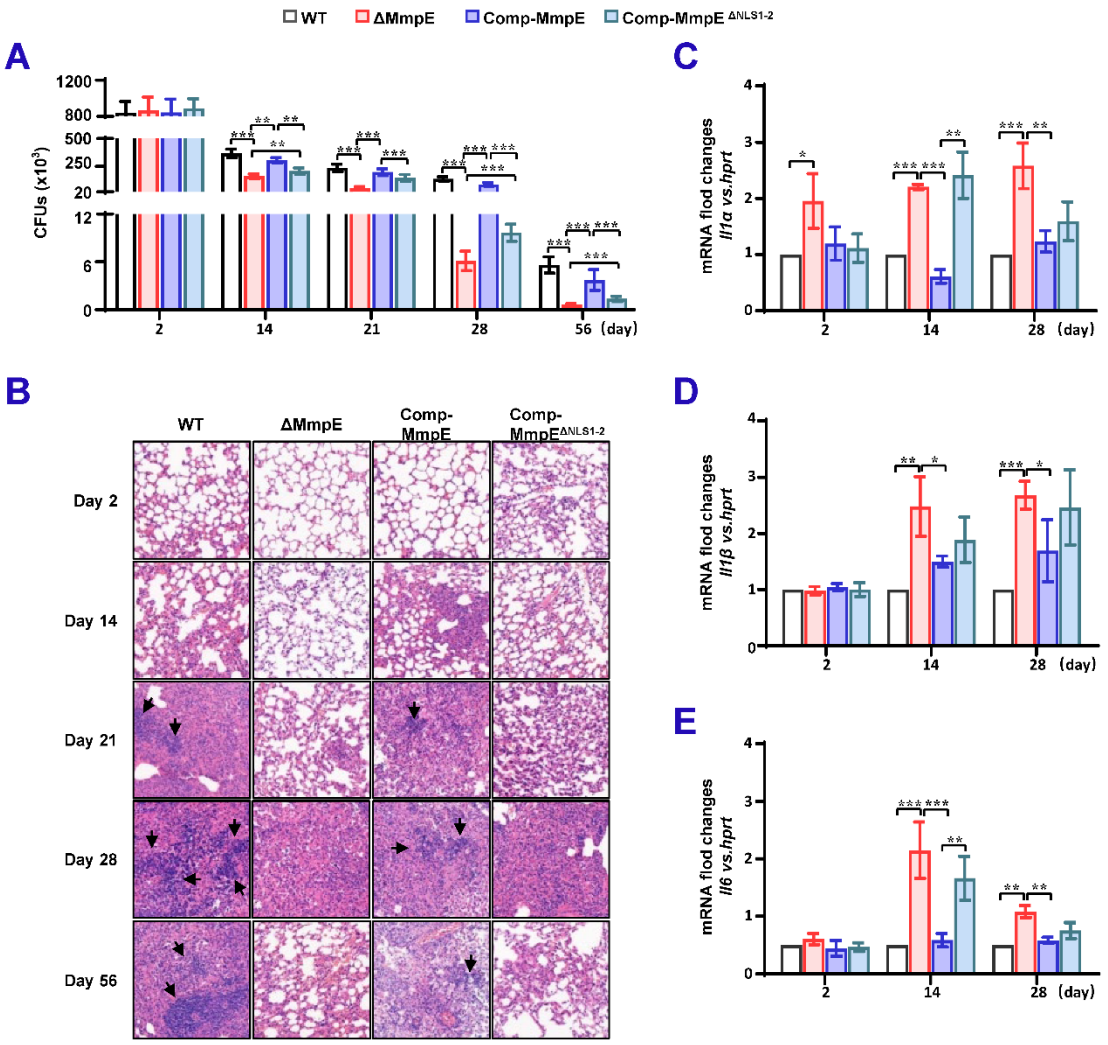

1063

1064 **Figure 6. Nuclear translocation of MmpE is essential for mycobacterial survival**
1065 **in mice.**

1066 (**A**) Bacterial burden in lungs of infected mice. Specific pathogen-free (SPF) C57BL/6
1067 mice (n = 6 per group) were intratracheally infected with 1.0 × 10^7 colony-forming units
1068 (CFU) of *M. bovis* BCG strains, including wild-type (WT), MmpE deleted (ΔMmpE),
1069 MmpE-complemented (Comp-MmpE), or MmpE-complemented with NLS-deleted
1070 variants (Comp-MmpE$^{\Delta NLS1\text{-}2}$). Bacterial titers in lung homogenates were quantified by
1071 CFU assays at 0,14,28, and 56 days post-infection.

1072 (**B**) Histopathology of infected lung tissues. Hematoxylin and eosin (H&E)-stained lung
1073 sections from mice infected as in (**A**) show granulomatous inflammation, Scale bars:
1074 200 μm.

1075 (**C-D**) Pro-inflammatory cytokine expression in the spleen of infected mice. qRT-PCR

analysis of cytokine mRNA levels of *Il1α* (**C**), *Il1β* (**D**)and *Il6* (**E**) in spleen tissues from infected mice (n = 6/group) at 2 to 28 days post-infection.

Data are presented as mean ± SD from six biologically independent experiments. Statistical significance was determined by a two-tailed unpaired Student's *t*-test (**P* < 0.05, ***P* < 0.01, ****P* < 0.001).

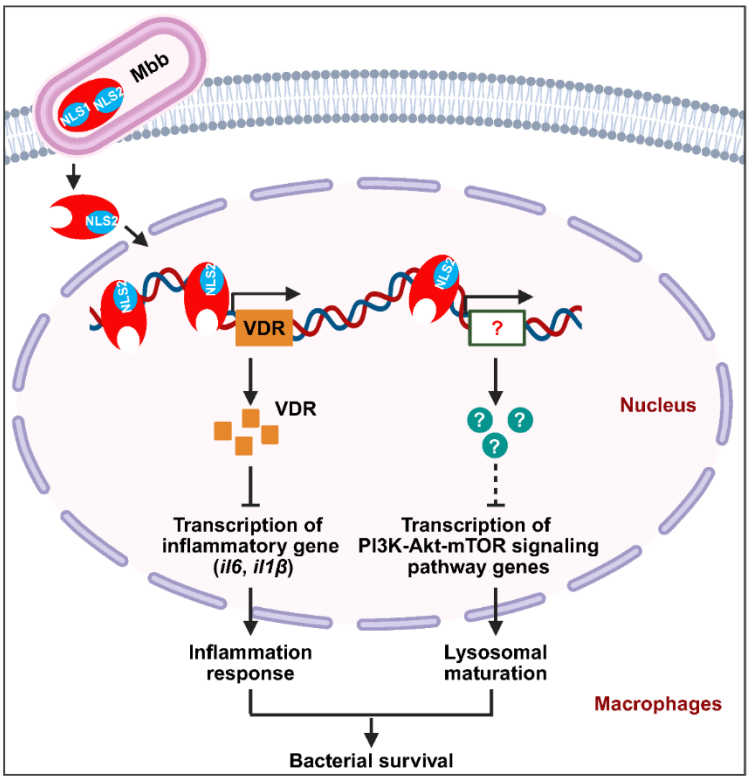

Figure 7. Schematic diagram of nucleomodulin MmpE-mediated immune suppression and mycobacterial survival.

Upon mycobacterial infection, MmpE translocates into the host cell nucleus via its NLS2 motif (RRK$^{460–462}$), where it binds to the promoter region of the *VDR* gene, repressing transcription of downstream inflammatory genes. Simultaneously, MmpE inhibits the PI3K–Akt–mTOR signaling pathway, leading to impaired phagosome maturation. These combined actions facilitate immune evasion and promote enhanced mycobacterial survival within macrophages and in mice.

1093 **Supplementary Figure Legend**

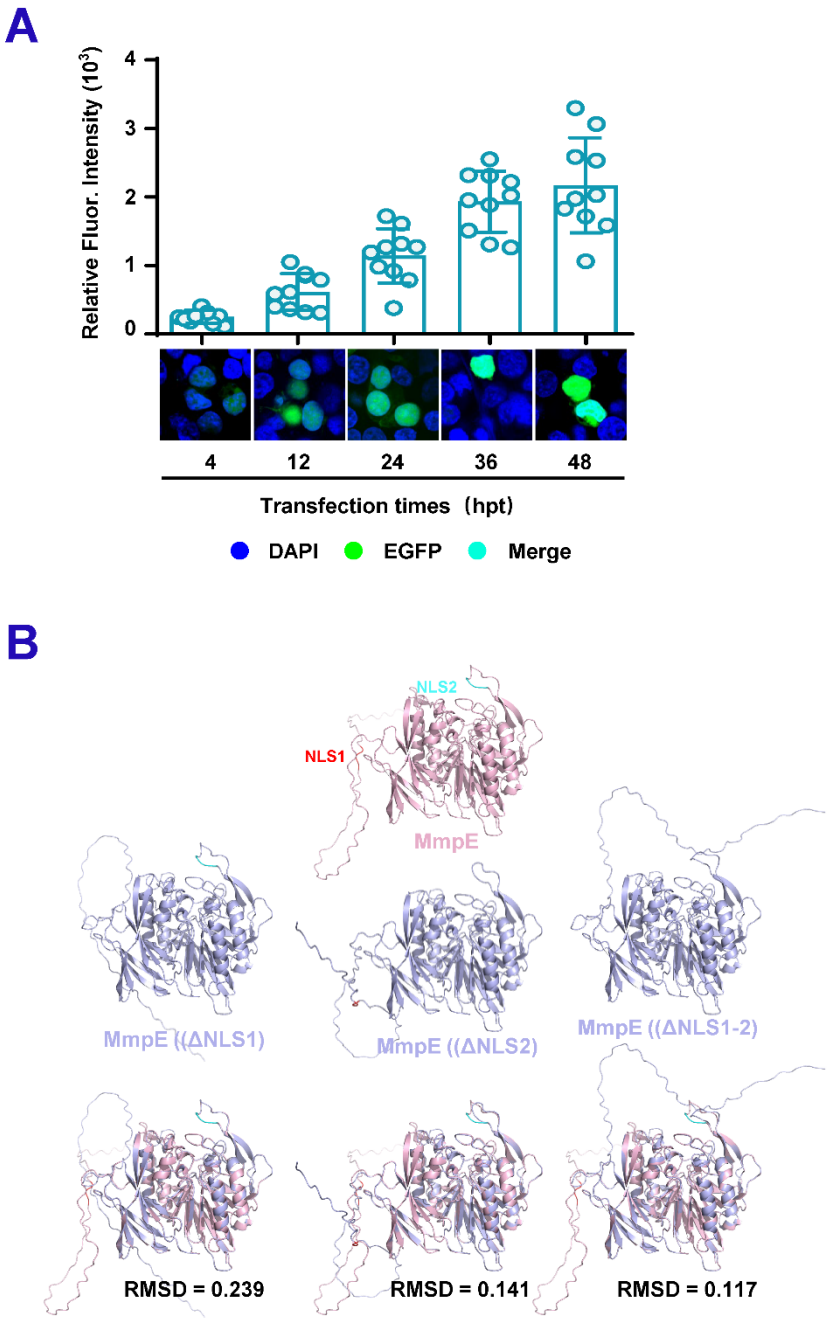

1094

1095 **Supplementary Figure 1. Identification of MmpE as a nucleomodulin in**
1096 **Mycobacterium.**

1097 (**A**) MmpE is a mycobacterial nucleomodulin. Subnuclear localization of MmpE-EGFP.
1098 Confocal microscopy was used to assess the nuclear distribution of MmpE-EGFP at
1099 various time points post-transfection. Nuclei were stained with DAPI (blue); MmpE-
1100 EGFP is shown in green. Scale bar: 10 μm.

(**B**) AlphaFold-predicted structural models of MmpE with NLS truncations. Structural models of MmpE were generated using AlphaFold 2.2.0 to assess the impact of NLS deletions on overall protein conformation. (upper) Full-length MmpE structure shown as a reference. (middle) MmpE structure with NLS deleted. (botten) Predicted structures of MmpE with individual deletions of NLS1, NLS2, or both motifs. Confidence scores (pLDDT) were used to evaluate prediction reliability, and UCSF ChimeraX was used to visualize and compare structural changes.

A

Protein Chain	Description	Z Value	RMSD Value
6py9-C	$Fe^{(3+)}$-$Zn^{(2+)}$ purple acid phosphatase	36.5	2.3
6py9-D	$Fe^{(3+)}$-$Zn^{(2+)}$ purple acid phosphatase	36.5	2.3
6py9-A	$Fe^{(3+)}$-$Zn^{(2+)}$ purple acid phosphatase	36.4	2.3
4kkz-C	purple acid phosphatase	36.3	2.3
4kkz-A	purple acid phosphatase	36.3	2.3
6g46-D	$Fe^{(3+)}$-$Zn^{(2+)}$ purple acid phosphatase	36.3	2.3
2qfp-B	purple acid phosphatase	36.3	2.3

Z value>10 and RMSD value<4 indicate that the comparison result is extremely reliable

B

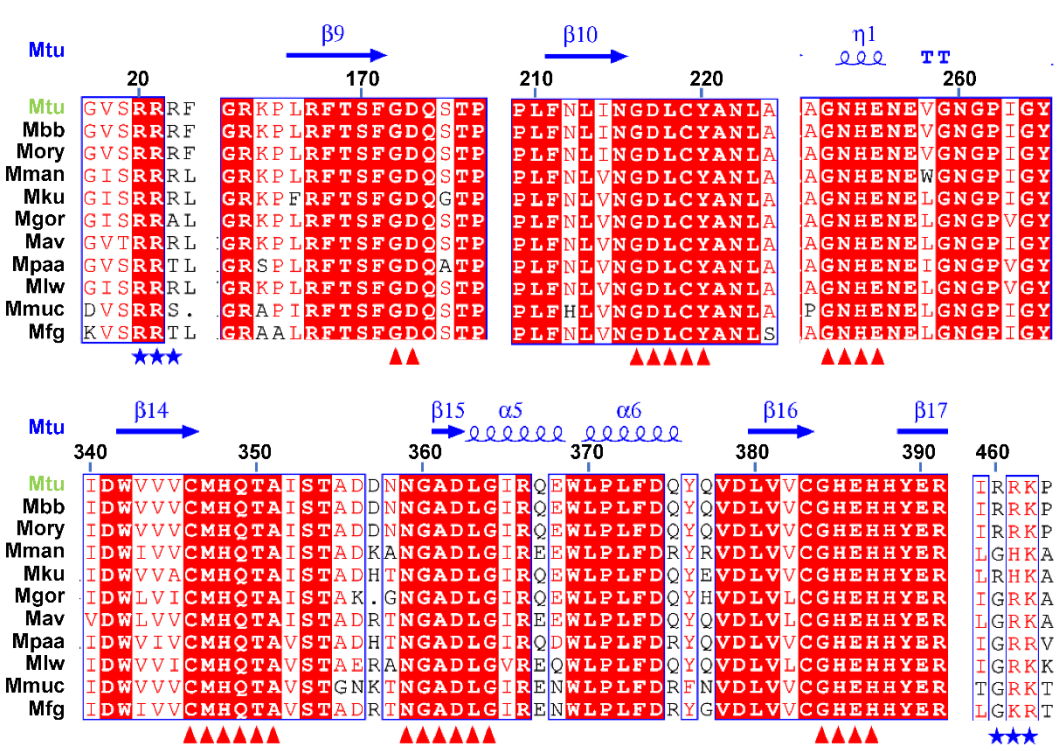

Supplementary Figure 2. Identification of MmpE as a conserved Fe^{3+}/Zn^{2+}-metallophosphatase in Mycobacteria.

(A) Sequence and structure-based analyses of MmpE. Sequence and structure-based analyses were performed using UCSF Chimera to investigate the potential function and structural features of MmpE. The structural comparison results, with a *Z* value >10 and RMSD value <4, indicate high confidence in the predicted structural models.

(B) Clustal Omega sequence alignment of MmpE from various mycobacterial species,

highlighting conserved residues (≥90% identity, shown in red). Blue stars indicate the predicted NLSs, and red triangles mark characteristic sequences found in metallophosphatases. Species abbreviations: *M. tuberculosis* (Mtu), *M. bovis* BCG (Mbb), *M. orygis* (Mory), *M. kubicae* (Mku), *M. paraterrae* (Mpaa), *M. farcinogenes* (Mfg), *M. mucogenicum* (Mmuc), *M. vicinigordonae* (Mgor), *M. lentiflavum* (Mlw), *M. avium* (Mav), *M. manitobense* (Mman).

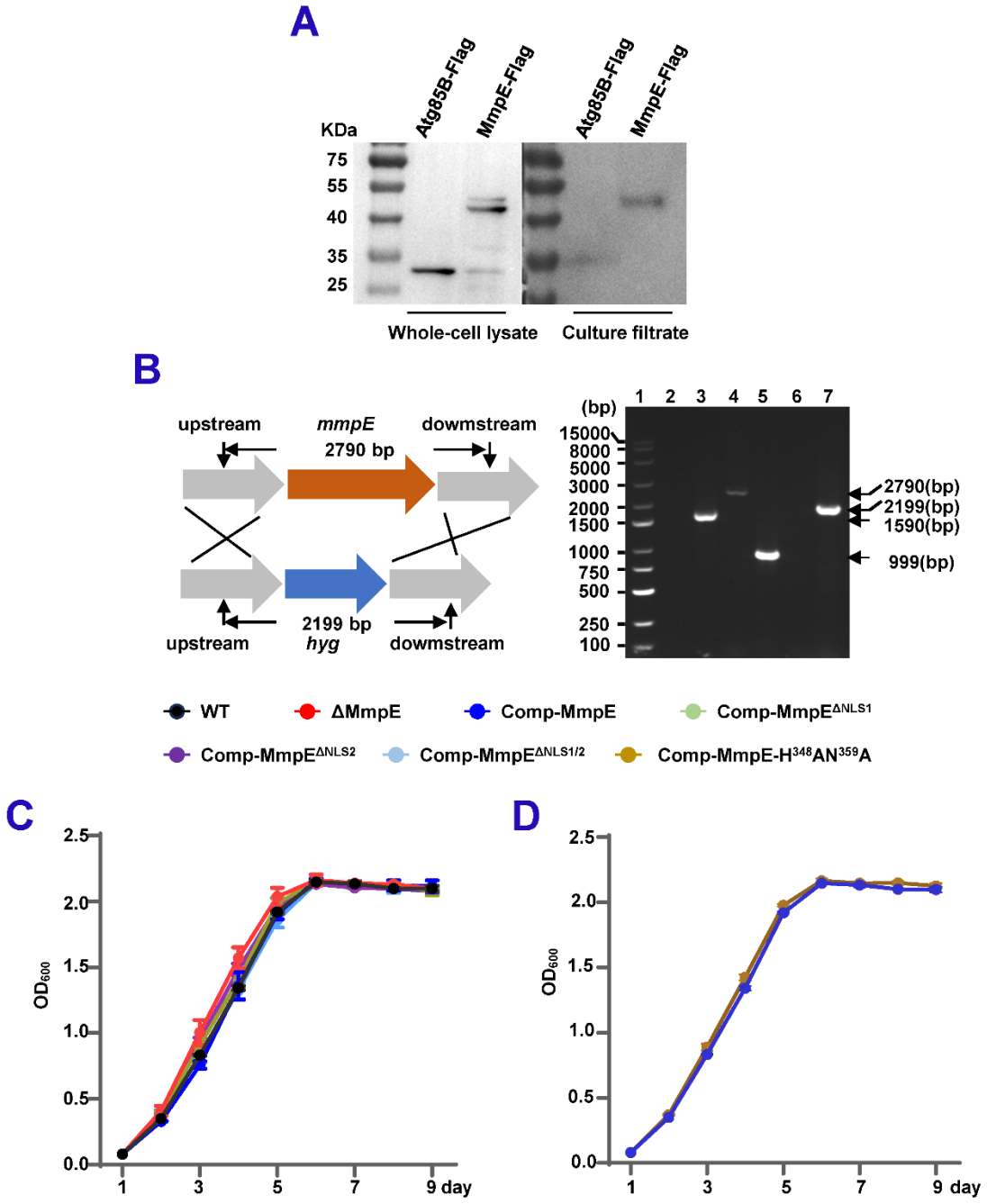

Supplementary Figure 3. The nuclear translocation and phosphatase activity of MmpE are essential for *M. bovis* BCG survival in macrophage cells.

(**A**) Detection of mycobacterial MmpE secretion ability. C-terminally 2×Flag-tagged Ag85B (positive control) and MmpE were expressed in *M. bovis* BCG strains. Immunoblot analysis of bacterial lysates and culture supernatants showing the expression and secretion of Flag-tagged Ag85B and MmpE.

(**B**) Construction and validation of the MmpE-deleted strain of *M. bovis* BCG. (left) Schematic diagram of the homologous recombination strategy used to delete *mmpE* from the *M. bovis* BCG genome. (right) Wild-type and mutant strains were used as templates to amplify the *mmpE* gene (600 bp upstream–600 bp downstream) by PCR. Lanes 1 and 3: wild-type genomic DNA; lanes 2 and 4: Δ*mmp*E genomic DNA.

(**C-D**) Growth curve analysis of BCG strains. Growth of *M. bovis* BCG strains, including wild-type BCG (WT), MmpE-deleted (ΔMmpE), MmpE-complemented (Comp-MmpE), and NLS-deleted complemented (Comp-MmpE$^{\Delta NLS1\text{-}2}$) strains(**C**), or phosphatase activity site mutation complement (Comp-MmpE-H^{348}AN^{359}H) (**D**), was measured in 7H9 medium.

Data are presented as mean ± SD from three biologically independent experiments. Statistical significance was determined by a two-tailed unpaired Student's *t*-test.

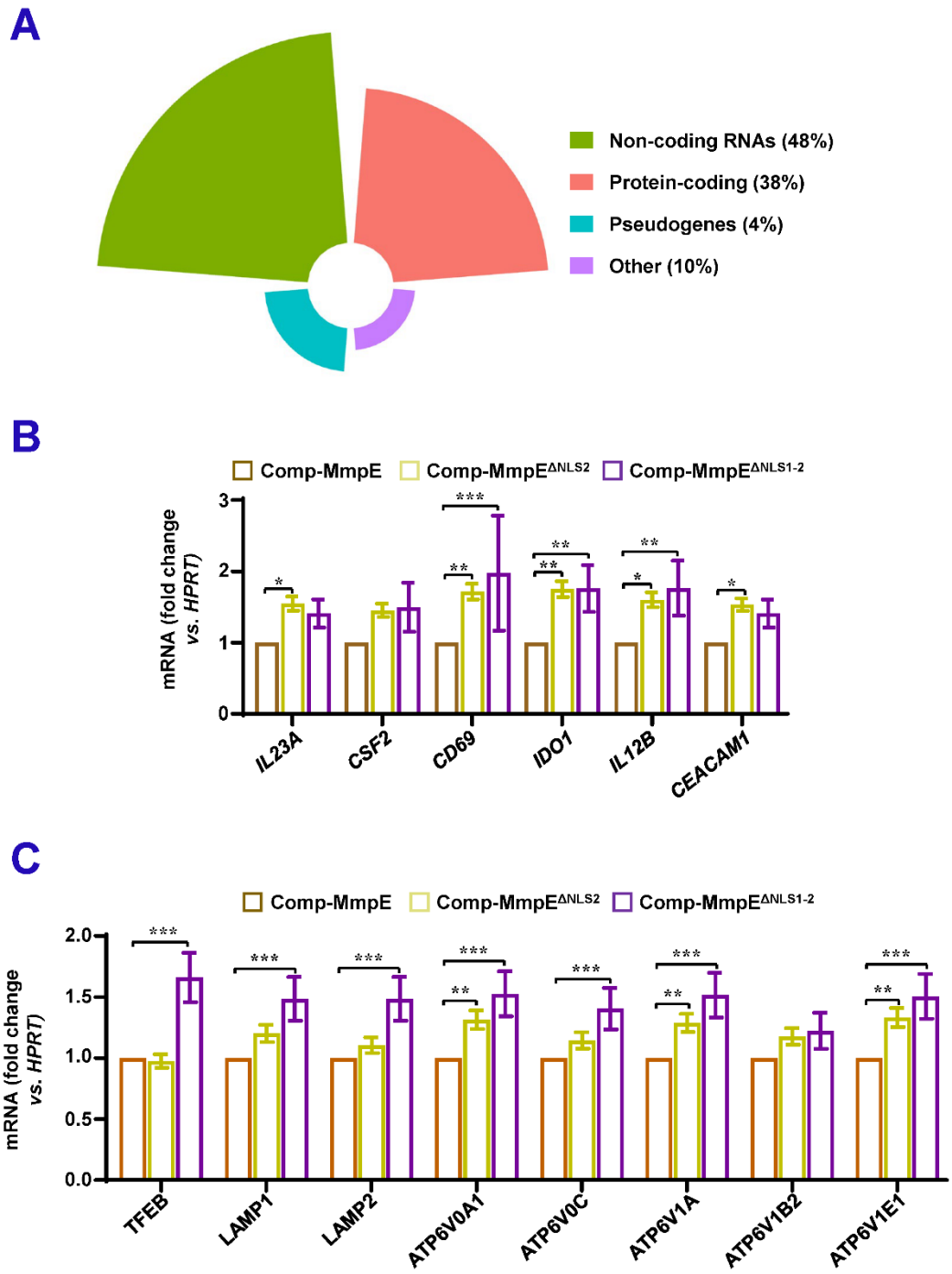

Supplementary Figure 4. MmpE modulates host transcription network involved in inflammation response and lysosomal maturation

(**A**) Biotype distribution of potential MmpE-regulating DEGs genes in THP-1 cells. (**B-C**) Quantitative RT-PCR analysis of gene expression in infected THP-1 cells. THP-1 cells were infected with complemented strain (Comp-MmpE) and NLS-deleted complemented (Comp-MmpE$^{\Delta NLS2}$, Comp-MmpE$^{\Delta NLS1-2}$) strains for 20 h. mRNA levels of cytokine genes (**B**); mRNA levels of genes involved in lysosomal acidification and

biogenesis (**C**).

Data are presented as mean ± SD from three biologically independent experiments. Statistical significance was determined by a two-tailed unpaired Student's *t*-test (**P* < 0.05, ***P* < 0.01, ****P* < 0.001).

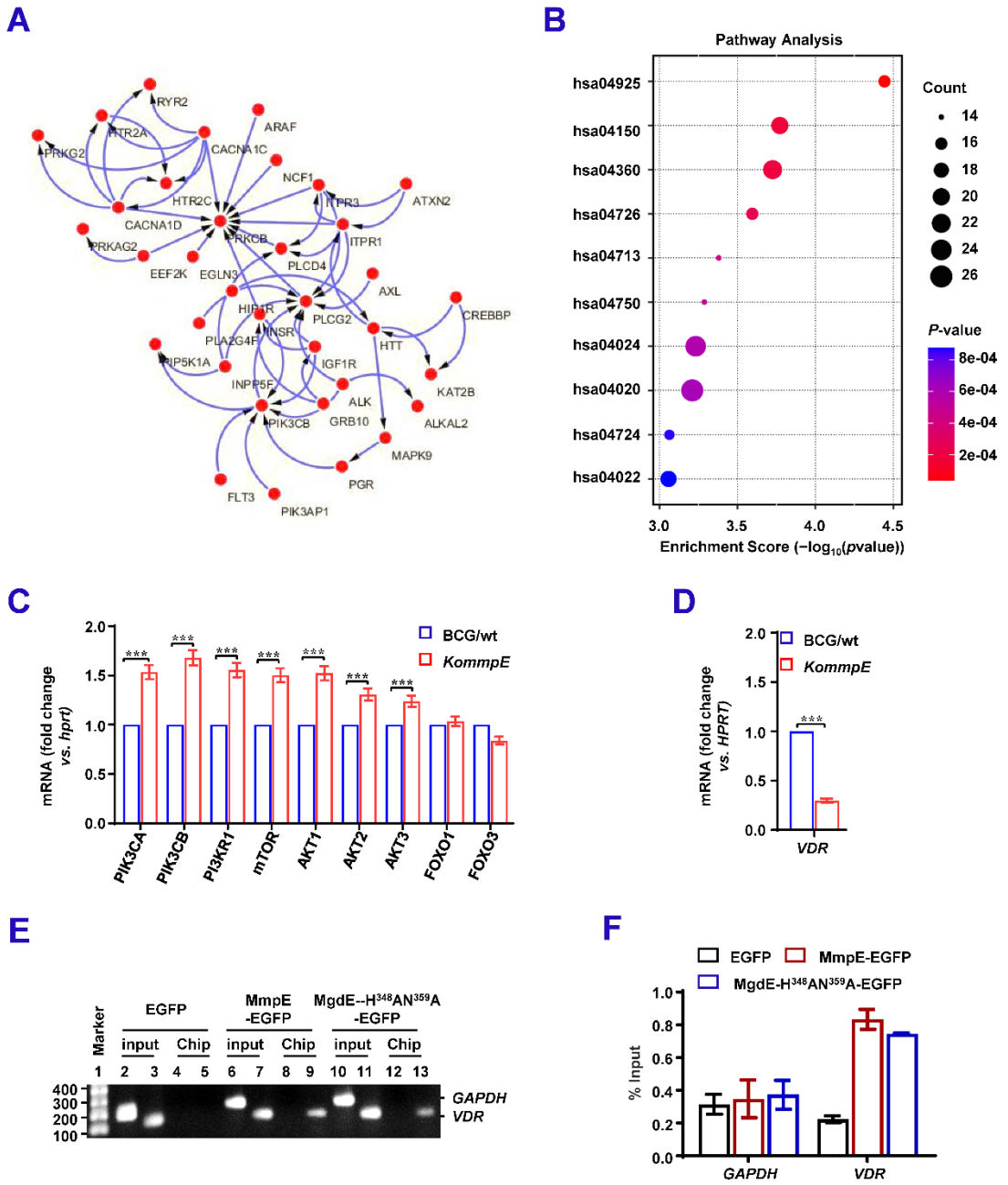

Supplementary Figure 5. MmpE suppresses the expression of *VDR* and inhibits activation of the PI3K–Akt–mTOR signaling pathway.

(A) Interaction network of DEGs associated with MmpE-binding sites. The network was constructed using STRING v12.0 and visualized with Cytoscape, highlighting

interactions between genes potentially regulated by MmpE.

(B) KEGG pathway enrichment analysis of MmpE-binding sites identified in EGFP-MmpE-transfected HEK293T cells revealed significant enrichment in multiple signaling pathways, including aldosterone-regulated sodium reabsorption (hsa04925), mTOR signaling (hsa04150), axon guidance (hsa04360), serotonergic synapse (hsa04726), circadian entrainment (hsa04713), inflammatory mediator regulation of TRP channels (hsa04750), cAMP signaling (hsa04024), calcium signaling (hsa04020), glutamatergic synapse (hsa04724), and cGMP–PKG signaling (hsa04022). The bar plot shows selected significantly enriched pathways. Bar length represents the number of MmpE-binding sites associated with each pathway, and the color gradient indicates statistical significance, represented as $-\log_{10}$(*P*-value).

(**C-D**) Quantitative RT-PCR analysis of gene expression in infected THP-1 cells. THP-1 cells were infected with wild-type BCG (BCG/wt), MmpE-deleted (*KommpE*) strains for 20 h. mRNA levels of PI3K-Akt pathway(**C**); mRNA levels of *VDR* gene (**D**).

(E-F) ChIP-PCR and qPCR analyses of *VDR* promoter binding by MmpE and the phosphatase-deficient mutant MmpE-$H^{348}AN^{359}A$ in HEK293T cells. Chromatin was immunoprecipitated from cells transfected with EGFP control, MmpE-EGFP, or MmpE-$H^{348}AN^{359}A$-EGFP constructs. PCR was performed using primers targeting the *VDR* promoter and *GAPDH* (negative control), and products were analyzed by agarose gel electrophoresis (**E**). ChIP enrichment for the *VDR* and *GAPDH* promoter regions was quantified by qPCR (**F**), with enrichment calculated using the $2^{-\Delta Ct}$ method.

Data are presented as mean ± SD from three biologically independent experiments. Statistical significance was determined by a two-tailed unpaired Student's *t*-test (***$P < 0.001$).

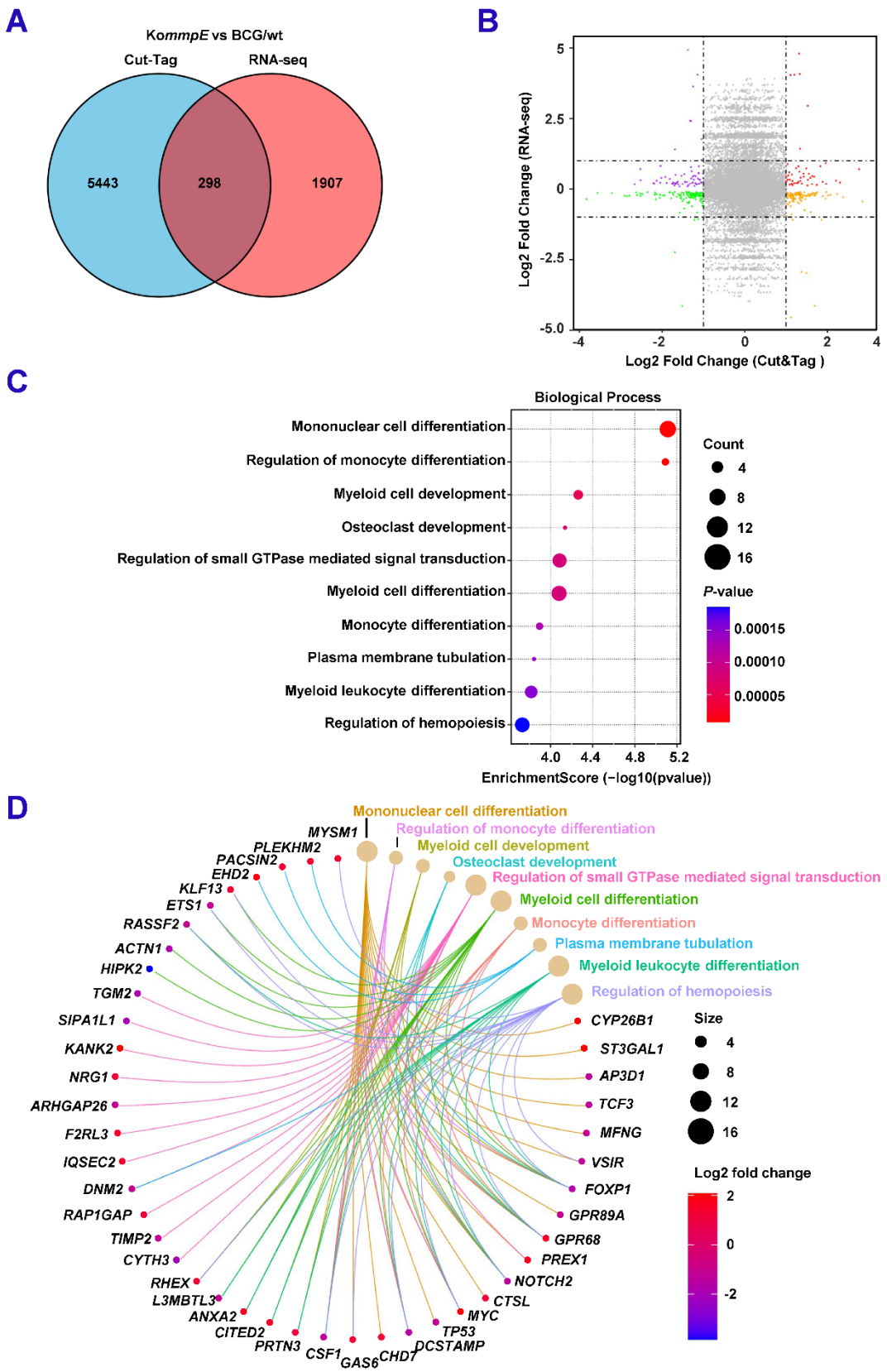

Supplementary Figure 6. MmpE modulates the transcription of immune-associated genes.

(**A**) Association between differentially expressed genes and differential peak-related

genes. Venn diagram showing the overlap between differential peak-related genes identified by CUT&Tag sequencing and DEGs identified by RNA-seq analysis.

(B) Four-quadrant scatter plot comparing CUT&Tag-seq and RNA-seq results. The $\log_2$(fold change) of peak-related genes from CUT&Tag-seq is plotted against the $\log_2$(fold change) of FPKM values from RNA-seq analysis. The scatter plot demonstrates the correlation between chromatin binding changes and gene expression levels.

(C) GO enrichment analysis of DEGs revealed significant overrepresentation of Biological Process (BP) terms in macrophages infected with Ko*mmpE* compared to those infected with wild-type BCG (BCG/wt).

(D) Chord plot showing significantly altered genes associated with GO Biological Process pathways in Ko*mmpE*-infected macrophages compared to BCG/wt infection.

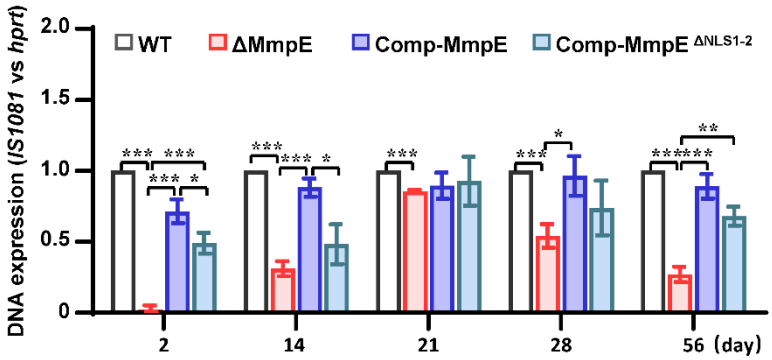

Supplementary Figure 7. MmpE promotes mycobacterial colonization in the spleen of mice.

Bacterial colonization in the spleen. CFU assays were performed on splenic homogenates from mice infected as described in Figure 6A. Bacterial loads (CFU/g tissue) were quantified at 2, 14, 21, 28, and 56 days post-infection. Data are presented as mean ± SD (n = 3). Statistical significance was determined using a two-tailed unpaired Student's *t*-test ($P < 0.05$, $^{**}P < 0.01$, and $^{***}P < 0.001$).